

# Spectral Analysis of the Lyman Alpha Forest in a Cold Dark Matter Cosmology

Yu Zhang<sup>1,2</sup>, Peter Anninos<sup>1</sup>, Michael L. Norman<sup>1,2</sup>, and Avery Meiksin<sup>3,4</sup>

<sup>1</sup>*Laboratory for Computational Astrophysics, National Center for Supercomputing Applications,  
University of Illinois at Urbana-Champaign, 405 N. Mathews Ave., Urbana, IL 61801*

<sup>2</sup>*Astronomy Department, University of Illinois at Urbana-Champaign, 1002 West Green Street,  
Urbana, IL 61801*

<sup>3</sup>*Department of Astronomy & Astrophysics, University of Chicago, 5640 South Ellis Avenue,  
Chicago, IL 60637*

<sup>4</sup>*Edwin P. Hubble Research Scientist*

## ABSTRACT

We simulate the Ly $\alpha$  forest in a standard CDM universe using a 2-level hierarchical grid code to evolve the dark and baryonic matter components self-consistently. We solve the time-dependent ionization equations for hydrogen and helium, adopting the Haardt & Madau (1996) estimate for the metagalactic UV radiation background. We compare our simulation results with the measured properties of the Ly $\alpha$  forest by constructing synthetic spectra and analyzing them using an automated procedure to identify, deblend, and fit Voigt line profiles to the absorption features. The H I column density and Doppler-parameter distributions we obtain agree closely with those measured by the Keck HIRES and earlier high spectral resolution observations over the column density range  $10^{12} \text{ cm}^{-2} < N_{\text{HI}} < 10^{16} \text{ cm}^{-2}$ . In particular, we find a power-law column density distribution persists to the lowest values ( $\sim 10^{12} \text{ cm}^{-2}$ ) reported from the HIRES measurements, in agreement with the incompleteness-corrected observations. We are able to match the normalization of the column density distribution at the low end using the Haardt & Madau spectrum and a baryon density consistent with nucleosynthesis limits. We find, however, a significant deficit of systems at higher column densities,  $N_{\text{HI}} > \text{few} \times 10^{16} \text{ cm}^{-2}$ . The deficit arises from a curvature in the column density distribution that may not be removed by an overall renormalization. We find evolution in the cloud number density and opacity comparable to the observed evolution, though growing somewhat too quickly at the highest redshifts. The evolution, however, is sensitive to the assumed UV radiation field, which becomes increasingly uncertain at higher redshifts ( $z > 3.5$ ). We also compare with measured values of the intergalactic He II opacity. Our results require a He II ionizing background lower than the Haardt & Madau estimate by a factor of 4, corresponding to a soft intrinsic QSO spectrum of  $\alpha_Q \approx 1.8 - 2$ .

*Subject headings:* cosmology: theory – dark matter – intergalactic medium; methods: numerical; quasars: absorption lines

## 1. Introduction

Since the identification of Ly $\alpha$  absorption lines in QSO spectra (Lynds 1971), and the first major survey of their properties (Sargent et al. 1980), the Ly $\alpha$  forest has been recognized as a unique probe of the physical state of the universe during the early stages of cosmic evolution. Studies of these absorption features offer several advantages over galaxies: (1) the lines are associated with typical structures as opposed to the “rare” structures (such as galaxies and clusters) which arise from the statistical tail of density perturbations; (2) they are observed along random directions in the sky and may not be biased with respect to the local structure distribution; (3) they are found at very high redshifts and thus probe the matter content at early times when the differences between competing cosmological models are most pronounced; and (4) they potentially comprise an enormous database with approximately  $10^3$  discovered QSOs with each QSO generating tens to hundreds of lines, presenting a distinctive statistical advantage compared to other astronomical observations. Using remote high-redshift QSOs as beacons through the intergalactic medium (IGM), the universe can be probed on much larger scales than allowed by existing catalogs of galaxies. They can be used both as tracers of the matter distribution and as probes of physical conditions in the universe at very early epochs when larger structures, such as galaxies, are still forming and evolving. Ly $\alpha$  clouds may be the missing link between primordial density fluctuations and the formation of galaxies and clusters of galaxies.

Early attempts to explain the Ly $\alpha$  forest lines attributed the absorption features to the hydrogen in intervening protogalaxies photoionized by a QSO-dominated UV background (Arons 1972), or to self-gravitating isothermal gas clouds (Black 1981), although the latter are gravitationally unstable over the range of column densities required. Bahcall & Salpeter (1965) argued that broad Ly $\alpha$  absorption features should appear due to intervening clusters of galaxies, though these have yet to be definitively detected. Ostriker & Ikeuchi (1983) (see also Ikeuchi & Ostriker 1986), following the lead of Sargent et al. (1980), subsequently formulated an elaborate theory of intergalactic clouds stabilized by the pressure of an external hot IGM. The virtue of this theory is that it provides several observational tests and predictions about both the IGM and the clouds themselves. However, the theory lacks a clear picture for the formation of Ly $\alpha$  clouds and ionization of the IGM. Shortly thereafter, the successes of the CDM model created an interest in combining this theory of large scale structure formation with the formation of Ly $\alpha$  clouds into a single unified picture. In this scenario, Ly $\alpha$  clouds can either be associated with bound structures, stabilized by the gravity of dark matter mini-halos (Rees 1986, 1988; Ikeuchi 1986), or with post-photoionized unconfined gas in low mass objects that developed from small mass fluctuations (Bond, Szalay, and Silk 1988).

These theoretical models, however, treat Ly $\alpha$  clouds as isolated objects and attempt only to explain their physical state and interactions with the environment. They do not provide a self-consistent framework for the formation, evolution, and interactions of the clouds, nor can any single analytical model account for the broad range of observed cloud properties. There are also inherent limitations to these models because of their underlying assumptions and simplifications; for example, neglecting or simplifying microphysical processes and the nonlinear interactions of the

small scale fluctuations which collapse at nearly the same time in CDM-like models.

The limited ability of analytic theories to account for the complexity and range of the observed properties of Ly $\alpha$  clouds and the IGM, combined with the rapid progress in numerical techniques, have motivated a number of attempts to study the formation and evolution of the intergalactic medium as a whole, in both clumpy and diffuse forms, by means of cosmological hydrodynamics/ $N$ -body simulations. The advantage of this approach is that it is not necessary to impose *a priori* any physical constraints on the clouds (i.e., pressure or gravity confinement) nor on their environments. Given a spectrum of primordial perturbations, the clouds form and evolve naturally under gravitational, hydrodynamic, thermal and chemical forces.

Three major cosmological simulations of QSO absorption line systems have been performed to date: The first Ly $\alpha$  simulation was performed by Cen et al. (1994) (see also Miralda-Escudé et al. 1996) in a flat CDM universe with a nonzero cosmological constant using a grid-based TVD hydrodynamics code. Zhang, Anninos, & Norman (1995), hereafter referred to as ZAN95, performed a self-consistent multi-species simulation in a CDM universe using a 2-level hierarchical grid code for higher resolution. Independently, Hernquist et al. (1996) performed a simulation of the standard CDM (SCDM) universe, but using a Smooth Particle Hydrodynamics (SPH) code. Significantly, all the calculations are able to recover the general statistical properties of the Ly $\alpha$  clouds, such as the column density and equivalent width distributions, Doppler parameters, and the size of the absorption features (Charlton et al. 1996). A theoretical paradigm is thus beginning to emerge from these calculations in which Ly $\alpha$  absorption lines originate from the small scale structure in pregalactic or intergalactic gas through the bottom-up hierarchical formation picture in a CDM-like universe. The absorption features originate in structures exhibiting a variety of morphologies, from fluctuations in underdense regions to spheroidal minihalos to filaments extending over scales of a few megaparsecs. A more detailed discussion of the morphologies and physical state of the systems found in our simulations is presented in Zhang et al. (1997).

In this paper, we follow up on our previous effort (ZAN95) to present a unified picture of the IGM and Ly $\alpha$  absorbers for a CDM universe. The results in ZAN95 are extended in §4 and §5 to include studies of the line center opacity, metal line systems, flux decrement calculations, and evolutions of the effective opacity and line number, in addition to presenting more detailed discussions of the Doppler parameters and column density and equivalent width distributions at a fixed redshift  $z = 3$ . A comprehensive discussion of the statistical correlation between the observed spectral properties of Ly $\alpha$  lines and the physical state of the absorbers will be presented in a companion paper (Zhang et al. 1997).

Furthermore, we note that the statistical analysis presented in ZAN95 was derived from data obtained directly from the physical properties of the baryonic gas in the simulation. Here we describe a new procedure we developed to more closely mimic observational methods. In particular, we have implemented a convolution algorithm to synthesize absorption spectra through the computational box, and developed a new analysis procedure to identify, deblend, fit and extract the

physical properties of absorption features in generated spectra. It should be pointed out that Cen et al. (1994) and Hernquist et al. (1996) also utilize a spectral method to synthesize and reduce spectra. However, they adopt a simplified “threshold” method and do not attempt to deblend lines in analyzing their spectral data. The failure to properly deblend lines will result in an overestimate of the Doppler widths of the lines. Their technique will also substantially undercount the lowest column density features in the spectra. More advanced methods of analysing spectral data, such as those introduced here, are required to better assess the agreement with the observed data. A similar approach has recently been adopted by Davé et al. (1997). Following the discussion of our numerical methods and simulations in §2, we present a detailed investigation of the different spectral analysis methods applied to our numerical data in §3. A detailed analysis of the derived statistics of the Ly $\alpha$  forest at  $z = 3$  is provided in §4, and of the evolution of the forest in §5. We summarize our results in §6.

## 2. The Simulations

Altogether, we have performed four separate simulations of the Ly $\alpha$  forest in a standard Cold Dark Matter (CDM) dominated universe using our 2-level hierarchical grid code HERCULES (Anninos, Norman, & Clarke 1994; Anninos et al. 1996). The different physical and computational parameters for each of the calculations are summarized in Table 1. Two different box sizes, each with two levels of nested grids, were considered: 3.2 and 9.6 Mpc, a reasonable compromise between resolving small scale structures, including larger scale power, and sampling a large enough volume to derive reliable statistics. The smaller 3.2 Mpc box simulations were discussed in ZAN95. Here we focus on the results from the larger 9.6 Mpc box, and merely reference and make passing comparisons to the smaller box results when appropriate.

Our model background spacetime is a flat, cold dark matter dominated universe with the initial density perturbations originating from inflation-inspired adiabatic fluctuations. The BBKS (Bardeen et al. 1986) transfer function is employed with the standard Harrison-Zel'dovich power spectrum. We adopt a fluctuation amplitude consistent with the present number density and temperatures of galaxy clusters (White, Efstathiou, & Frenk 1993; Bond & Myers 1996), although we also compare with the earlier high amplitude model. While the CDM power-spectrum is known not to be able to match both the clustering of galaxies at small scales and the measurements of COBE at large, it adequately represents the power-spectrum over the range of scales of interest to the Ly $\alpha$  forest problem. The baryonic fraction  $\Omega_b$  is chosen so that  $\Omega_b h^2$  is consistent with the latest results from Big Bang nucleosynthesis (Copi, Schramm, & Turner 1995), and the baryonic fluid is composed of hydrogen and helium in primordial abundance with a hydrogen mass fraction of 76%. We use the COSmological initial conditions and MICrowave anisotropy codeS (COSMICS, Bertschinger 1995) to generate the initial particle positions and velocity perturbations appropriate to the particular parameters in the large box simulations. The cosmological model parameters used in our different simulations are provided in Table 1.

For the most part, the statistical analysis of the Ly $\alpha$  forest is performed with the top grid evolution as it contains a greater sample or range of data. However, to explore the effects of grid resolution, we take advantage of the 2-level nature of our code and introduce a second, more finely resolved, grid to cover a sub-region of the coarser top grid. In all our simulations, we use  $128^3$  cells on both the top and subgrids;  $64^3$  dark matter particles were used in the small 3.2 Mpc box simulation. However, the larger box calculation included  $128^3$  dark matter particles to verify that the particle sampling does not significantly affect the fluctuations in the cosmic voids. The subgrid is centered on the *least* dense region of the top grid for the purpose of resolving in greater detail the lowest column density absorbers which are found in the voids (Zhang et al. 1997). The refinement factor (the ratio of cell sizes between the top and sub grids) is 4 for all the subgrid simulations, yielding an effective grid resolution of  $512^3$  cells. Table 1 also lists the spatial and mass resolutions for both the top and subgrids of the different simulations. The characteristic length scale of the Ly $\alpha$  forest clouds, both observed and simulated, is typically a hundred or more kiloparsecs (Smette et al. 1995; Dinshaw et al. 1995; Fang et al. 1996; Charlton et al. 1996; Hernquist et al. 1996), and it is generally believed that their typical mass is of order  $10^7 - 10^9 M_\odot$ . Table 1 clearly demonstrates that our numerical setup has more than sufficient spatial and mass resolution to probe scales smaller than the typical Ly $\alpha$  clouds.

In addition to the usual ingredients of baryonic and dark matter, we also solve the coupled system of non-equilibrium chemical reactions with radiative cooling. The reaction network includes a self-consistent treatment of the following six species: H I, H II, He I, He II, He III and  $e^-$ . Details of the chemical model, cooling rates and numerical methods can be found in Abel et al. (1996) and Anninos et al. (1996). A final but essential component introduced in our simulations is an ultraviolet (UV) radiation background to ionize the otherwise neutral intergalactic medium. The intergalactic clouds are optically thin at the Lyman edge for column densities smaller than about  $N_{\text{HI}} = 8 \times 10^{16} \text{ cm}^{-2}$  (corresponding to  $\tau_L \approx 0.5$ , where  $\tau_L$  is the H I opacity at the Lyman edge). Hence, for the range of column densities we are interested in, the optically thin limit is a good approximation, i.e. it is not necessary to account for self-shielding of the external ionizing radiation field. The radiation background is also assumed to be uniform which is a fairly good approximation if one is mainly interested in the statistical properties of the Ly $\alpha$  absorbers.

A simple though somewhat arbitrary parameterization of the UV background radiation field  $J_\nu$  is a power law:  $J_\nu = J_L(\nu/\nu_L)^{-\alpha}$ , where  $\nu_L$  is the H I frequency at the Lyman edge and the spectral index  $\alpha$  is in the range 1 to 2. The amplitude of the radiation intensity is measured to be  $10^{-22 \pm 1} \text{ erg s}^{-1} \text{ cm}^{-2} \text{ Hz}^{-1} \text{ sr}^{-1}$ , according to the QSO proximity effect (Bajtlik, Duncan, & Ostriker 1988; Lu et al. 1997). The redshift dependence of the amplitude and the epoch at which the radiation is turned on must also be specified. Such a parametric prescription was utilized in our ZAN95 simulations.

Haardt & Madau (1996), however, have recently computed the UV radiation field with radiation transfer in a clumpy universe, based on the measured luminosity function of QSOs. The field is found as the self-consistent solution of the combined system of QSO sources, absorption by

the Ly $\alpha$  forest and Lyman limit systems, and reemission of the recombination radiation from the absorbing clouds. The photoionization rates  $\Gamma$  are provided by Haardt and Madau. We use their spectra to generate the photoionization heating rates, and fit them to the same functional form as Haardt and Madau adopt for the photoionization rates. These are shown plotted in Figure 1. We use the fits for the photoionization and photoionization heating rates in this paper. Since the cloud temperatures are not very sensitive to the assumed heating rate, we note that comparisons of our current results with those in ZAN95 can be made by simply rescaling by the ratio of radiation intensities, or more precisely, by the ratio of parameters  $\Omega_b^2/\Gamma$ , where  $\Gamma$  is the photoionization rate for the species of interest (see §4.1). The temperature is somewhat dependent on the gas density (Meiksin 1994; Croft et al. 1997), but for a limited range in  $\Omega_b$  (a factor of about 2), this is an approximately valid procedure, provided the regions have not undergone significant recombination into neutral hydrogen or neutral or singly ionized helium.

### 3. Spectral Analysis Methods and Tests

To compare the simulation results with the measured properties of the Ly $\alpha$  forest, it is desirable to mimic the observed data and its analysis as closely as possible. To do so, however, would entail building a sophisticated spectral simulation procedure that includes the vagaries of the actual data. This would require modeling the noise in the sky-subtracted spectra, the variations in the QSO spectrum through the forest, continuum fitting, and accounting for the finite resolution of the detectors. Rather than embarking on a massive simulation program at this stage, we instead concentrate on extracting the actual underlying statistical distributions of the absorber spectral properties that would be found from “perfect” observations. The belief is that the two distributions should coincide for optically thick (at line center) systems that are not too badly saturated, though they may deviate for the weaker optically thin systems. For the latter, we rely on the Monte Carlo simulations performed by the observers to test their success in recovering the weakest lines to evaluate the ability of the simulations to match the observational data. In this section, we describe the methods we have developed to generate and analyze our spectra. We also compare the results of our analysis method, which is based on Voigt profiles, against the threshold approach, as the latter was adopted in the most comprehensive treatments of the properties of the forest in previous simulations.

#### 3.1. Generating Spectra from Numerical Data

Ly $\alpha$  absorption in the spectrum of a QSO located at redshift  $z$  is calculated by  $e^{-\tau_\nu}$ , where the optical depth  $\tau_\nu$  is given by

$$\tau_\nu(t) = \int_t^{t_0} n_{\text{HI}}(t) \sigma_\nu c dt , \quad (1)$$

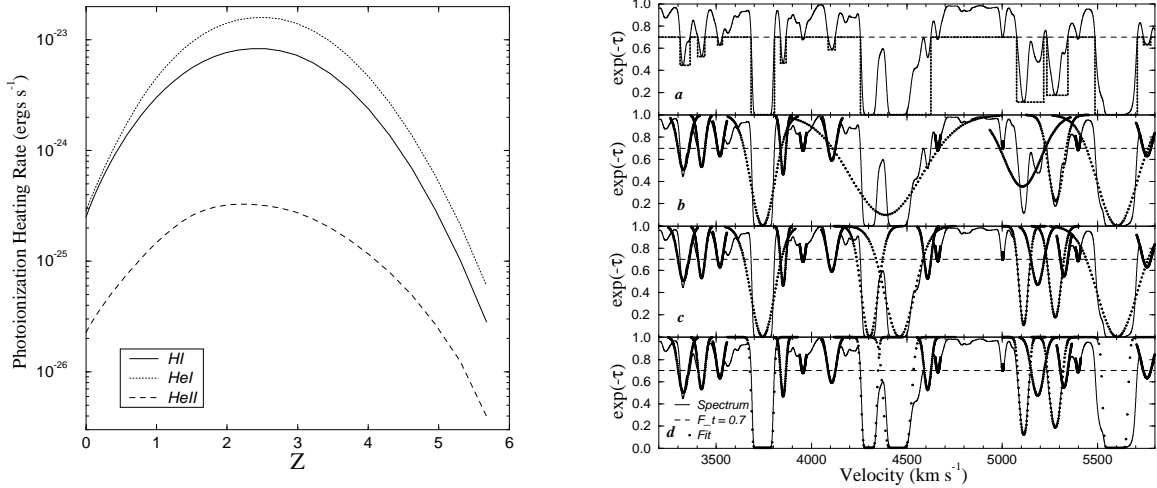


Fig. 1.— Photoionization heating rates per atom as a function of redshift for H I, He I, and He II from the Haardt and Madau (1996) radiation field.

Fig. 2.— Comparison of the different spectral line analysis methods: (a) the threshold method without profile fitting; (b) the threshold method with profile fitting; (c) the deblending method applied to the spectral data; and (d) the deblending method applied to the opacity data. The solid lines are the actual spectra, generated at  $z = 3$ , and the dots represent the identified lines and their fitted profiles. The horizontal dashed lines indicate the spectral cutoff used in this example,  $F_t = 0.7$ .

and the integration is performed along the line of sight between the QSO and observer. Here  $c$  is the speed of light,  $n_{\text{HI}}$  the number density of the H I absorbers, and  $\sigma_\nu$  the absorption cross-section which can be expressed as a Voigt function (Spitzer 1978),

$$\sigma_\nu = \sigma_0 V \approx \frac{\sigma_0}{\sqrt{\pi}\Delta\nu_D} \exp \left[ -\frac{(\nu - \nu_0)^2}{(\Delta\nu_D)^2} \right] + \frac{\sigma_0\Delta\nu_{\text{Lor}}}{2\pi(\nu - \nu_0)^2}, \quad (2)$$

where  $\nu_0$  is the Ly $\alpha$  rest frequency,  $\sigma_0 = (\pi e^2/m_e c) f$  is the resonant Ly $\alpha$  cross section and  $f$  is the upward oscillator strength.

In the first term of equation (2),  $\Delta\nu_D$  is proportional to the full width half maximum of the Gaussian profile due to the Doppler broadening which dominates the profile core

$$\Delta\nu_D = \nu_0 \frac{b}{c} = \nu_0 \sqrt{\frac{2kT}{m_p c^2}}, \quad (3)$$

where  $T$  is the gas temperature,  $k$  Boltzmann's constant and  $m_p$  the proton mass. The second term in equation (2) accounts for the asymptotic behavior of the Lorentzian wings of the profile as a result of radiation damping. The full width half maximum of the Lorentzian profile is given by

$$\Delta\nu_{\text{Lor}} = \frac{4\pi e^2}{3m_e c^3} \nu_0^2 f \approx 4 \times 10^{-23} \nu_0^2 f \text{ Hz}. \quad (4)$$

Since the Lorentzian wing is negligible for lines with equivalent width  $W_0 \leq 1 \text{ \AA}$  and column density  $N_{\text{HI}} \leq 10^{19} \text{ cm}^{-2}$ , we may use the Doppler term alone for the low and medium column density H I absorption lines. The radiation damping wings, however, can be significant for the He II lines, so a full Voigt profile is used in these cases.

Equation (1) can then be parameterized, to order  $v/c$ , by the redshifted frequency  $\nu$  as (see also Bi, Ge, & Fang 1995)

$$\tau_\nu(z) = \frac{c^2 \sigma_0}{\sqrt{\pi} \nu_0} \int_z^{z_0} \frac{n_{\text{HI}}(z')}{b} \frac{a^2}{\dot{a}} \exp \left\{ - \left[ (1+z') \frac{\nu}{\nu_0} - 1 + \frac{v}{c} \right]^2 \frac{c^2}{b^2} \right\} dz'. \quad (5)$$

Here,  $v$  is the peculiar velocity (coherent and turbulent) along the line-of-sight (LOS) which produces a shift at the line center relative to the Hubble velocity, and contributes to the line broadening together with the thermal motion. The cosmological expansion rate in equation (5) is given by the Friedman equation for the cosmological scale factor  $a$ ,

$$\dot{a} = H_0 \sqrt{1 + \Omega_0 z + \Omega_\Lambda (a^2 - 1)}. \quad (6)$$

To synthesize an absorption spectrum over a large redshift interval, say from  $z = 3$  to  $z = 0$ , we divide this redshift range into equal intervals of  $\Delta z = 0.1$  (the smallest practical interval at which we have retained data from the 3D simulations). A LOS is chosen randomly and the integrated optical depth (and absorption spectrum) is computed from equation (5) for different

values of redshifted frequency  $\nu$  in each redshift interval. To resolve the smallest spectral features present in our simulations, we use 50000 points to cover the range  $\Delta z = 0.1$ . The redshift interval corresponding to a physical length scale at any redshift  $z$  is given by

$$\delta z = 3.34 \times 10^{-4} \frac{Lh}{a} \sqrt{\Omega_0 z + \Omega_\Lambda(a^2 - 1) + 1}, \quad (7)$$

where  $L$  is the comoving box size in units of Mpc. For example, at redshift  $z = 3$  in an  $\Omega_0 = 1$  universe, equation (7) indicates that a box size of 9.6 Mpc corresponds to a redshift interval of  $\delta z = 1.3 \times 10^{-2}$ . Hence, each LOS samples the structures in the same cube approximately eight times over the interval  $\Delta z = 0.1$ . However, choosing a random orientation vector assures that each LOS samples the cube uniformly and does not bias the synthesized spectra in any significant way.

Table 2 lists the redshift, velocity and wavelength resolutions of our numerically generated spectrum, along with the corresponding resolutions of real observation instruments. Our spectral resolution is quoted in redshift space and is constant for all redshifts:  $\Delta z = \Delta v/c = 0.1/50000 = 2 \times 10^{-6}$ . This resolution is more than adequate to cover the grid cell intervals, which, at  $z = 3$ , are  $\Delta z = 1 \times 10^{-4}$  and  $2.5 \times 10^{-5}$  for the top and sub grids respectively. Keck/HIRES is the High Resolution Echelle Spectrograph installed on the 10-meter Keck telescope, and KPNO/KPE is the Kitt Peak Echelle spectrograph on the 4-meter Mayall telescope at the Kitt Peak National Observatory. These two spectrographs have obtained the bulk of the high resolution H I Ly $\alpha$  data to which we will be comparing our numerical results. ASTRO-2/HUT is the Hopkins Ultraviolet Telescope aboard the ASTRO-2 shuttle mission launched in 1994. HST/FOC is the Faint Object Camera aboard the Hubble Space Telescope launched in 1990. These two instruments have detected intergalactic He II absorption along the lines-of-sight to two QSOs (Davidsen, Kriss, & Zheng 1996; Jakobsen et al. 1994).

### 3.2. Line Analysis

Finding and fitting the absorption lines requires assumptions to be made regarding the shapes of the line profiles. Ideally, one would like to characterize the physical properties of the clouds imposing as little prejudice as possible. In order to avoid imposing a specific profile unnecessarily, Miralda-Escudé developed a “threshold”-based method of spectral analysis (Hernquist et al. 1996; Miralda-Escudé et al. 1996). This method identifies lines as regions in the spectrum  $e^{-\tau_\lambda}$  below a certain transmission threshold and computes the properties of these lines, such as the equivalent width and column density, using only the data below the threshold. Specifically, they evaluate the following integrals for the equivalent width and column density, respectively

$$W_0 = \int_{\lambda_1}^{\lambda_2} (1 - e^{-\tau_\lambda}) \frac{d\lambda}{1+z}, \quad (8)$$

$$N_{\text{HI}} = \int_{\lambda_1}^{\lambda_2} \frac{(1+z)c\tau_\lambda d\lambda}{\sigma_0 \lambda^2}, \quad (9)$$

where  $\lambda_1$  is the down-crossing wavelength where the transmission drops below the threshold, and  $\lambda_2$  is the up-crossing wavelength where the transmission rises above the threshold with  $\lambda_2 > \lambda_1$ . This method has the advantage of simplicity, permitting many lines to be identified and evaluated efficiently. It also has the merit of not assuming any particular line profile (except to compute the Doppler parameter  $b$ , a Voigt profile must effectively be adopted). For small line densities (at low redshifts) and with sufficiently low transmission thresholds, this method is an effective means for measuring the line properties.

For narrow and weak lines which are not blends, however,  $W_0$  and  $N_{\text{HI}}$  can both be underestimated if too low a spectral threshold is chosen, since the contribution from above the cutoff is not counted in the integrals. In addition, since no deblending is attempted to help isolate distinct components,  $W_0$ ,  $N_{\text{HI}}$  and  $b$  can be overestimated in the case of broad lines that are mostly blends. In fact,  $W_0$ ,  $N_{\text{HI}}$  and  $b$  are to first approximation the sums of the individual components making up the line complex. The first problem may be alleviated by setting a high transmission threshold. But this comes at the expense of introducing more blended lines, exacerbating the second problem. Table 3 (discussed in detail below) shows that overestimates of the line widths are much greater than underestimates associated with too low a threshold. Attempting to use a very low value for the threshold to avoid too many blends, however, would result in missing most of the narrow and low column density lines.

With the arrival of high resolution observational data and a larger database of lines at higher redshifts, it is essential to develop an alternative spectral reduction algorithm that is better suited to dealing with strong blending as well as being able to identify most of the individual absorption features in the spectrum for high transmission cutoffs. A line deblending procedure is essential to extract meaningful statistics and to make a full comparison with the new high resolution observational spectra. While a comparison with integrated absorption properties of the spectra may be made without line-identification, the lines contain a wealth of detailed information concerning the structure of the spectra. A complete comparison should include the effect of systematics and errors as closely as possible to those of the observed spectra. At present this is beyond the scope of the paper, though we anticipate making such a comparison in the future. Our present attempt is to analyze the spectra under ideal observing conditions. Indeed, it is the ideal results that the observer attempts to extract from his or her spectra, often including Monte Carlo simulations to correct for systematics (e.g., Hu et al. 1995).

We have developed a new procedure to identify the absorption lines above a specified opacity threshold (or below a spectral threshold) and to deblend the identified absorption features into individual and isolated lines using the sign and value of the local derivatives of the opacity (or transmission) with respect to the wavelength. The use of extrema allows one to identify local features within larger ones without relying on the spectrum to cross the transmission threshold. While the method is not foolproof — it may still miss weak lines superimposed on the wings of much stronger ones — it represents a significant improvement over the simple threshold method, especially for the lower column density systems.

After an individual line is identified and isolated, the rest-frame equivalent width can be computed using equation (8), performing the integration over the full line profile and not just over the region beneath the threshold. In order to extrapolate the data above the threshold and up to the continuum, a line profile needs to be assumed. The  $W_0$  thus computed has the advantage of being directly comparable to observations, but at the price of assuming a particular shape for the line profile. For the high transmission cutoff that we adopt ( $F_t = 0.95$ ), the contribution to  $W_0$  from above the threshold is negligibly small (because of the exponential drop in the Gaussian tail) and the integration over the region under the threshold is a good approximation to the true equivalent width provided the feature under the threshold is deblended.

To facilitate a comparison with the measured line properties, we follow the observers in adopting a Voigt profile. For lines with H I column densities smaller than  $10^{19}$  cm $^{-2}$ , the radiation damping wings contribute negligibly to the profile. Accordingly, we simplify the analysis by adopting a Doppler profile. The Doppler parameter  $b$  of each line can be obtained in one of two ways: either by fitting the isolated spectral (or opacity) profile with a Doppler function and deriving  $b$  from the line width, or using the following formula relating  $b$  to  $W_0$  (Spitzer 1978),

$$b = \frac{W_0 c}{2\lambda_0 F(\tau_0)}, \quad (10)$$

where  $\lambda_0$  is the H I Ly $\alpha$  rest wavelength,  $\tau_0$  is the optical depth at line center, and

$$F(\tau_0) = \int_0^\infty \left[ 1 - \exp(-\tau_0 e^{-x^2}) \right] dx \quad (11)$$

is the curve of growth function for a Maxwellian velocity distribution, which can be found tabulated in Spitzer (1978). For unsaturated lines  $F(\tau_0) \propto \tau_0$ , and the equivalent width is on the linear part of the curve of growth, i.e.  $W_0 \propto N_{\text{HI}}$ , independent of  $b$  (since  $\tau_0 \sim N_{\text{HI}}/b$ ). For saturated lines  $F(\tau_0) \propto (\ln \tau_0)^{1/2}$ , and the equivalent width is on the flat part of the curve of growth, i.e.  $W_0 \propto b(\ln \tau_0)^{1/2}$ , increasing slowly with  $N_{\text{HI}}$ . We find that the two determinations of the Doppler parameter typically agree to within a percent. We employ the first method for our data analysis. The column density is then determined from the line center opacity and Doppler parameter using (Spitzer 1978),

$$N_{\text{HI}} = \frac{\sqrt{\pi} \tau_0 b}{\sigma_0 \lambda_0}. \quad (12)$$

We note that either the opacity  $\tau_\lambda$  or the transmission  $e^{-\tau_\lambda}$  can be used in the spectral reduction procedure. We have tried both and found the differences to be negligible for unsaturated lines. However, for strongly saturated lines ( $N_{\text{HI}} \gtrsim 10^{14}$  cm $^{-2}$ ), the opacity data is needed to obtain a good fit to the individual lines because the large opacity causes the transmission to be vanishingly small and to resemble a square well, making it more difficult to fit properly (compare Figures 2c and 2d). In this regard, we differ from Davé et al. (1997) who confine their spectral analysis to the transmitted flux. Davé et al. (1997) instead adopt an approach that more closely mimics the observational procedure by decomposing their synthetic spectra, in which they have incorporated

noise and instrumental effects, into lines that match the spectrum as closely as possible. Under an ideal observational arrangement, the two approaches should agree. Observers attempt to “correct” for the resulting incompleteness and biases introduced into the deduced line lists through Monte Carlo simulations of their analysis procedure (e.g., Hu et al. 1995). We will therefore compare with the results of the observers including their Monte Carlo corrections when possible.

The described procedures of line finding and fitting have been fully automated and combined into a spectral reduction package which is fast and efficient enough to analyze thousands of lines in just a few minutes on a workstation.

### 3.3. Comparison of Methods

To test the accuracy of our spectral reduction method, we compare results from the different analysis techniques to the same synthetic spectrum. Figure 2 shows the differences between applying four variations of the methods to the same numerical spectrum of length  $2500 \text{ km s}^{-1}$  at  $z = 3$ . A transmission cutoff of  $F_t = 0.7$  is used in all cases. The solid lines are the raw spectral data and the dots represent the identified and fitted lines. Panel (a) is the threshold method with no deblending and no Voigt profile fitting. Panel (b) is the same as (a) except that each of the lines identified with the threshold method have been fitted to a Voigt profile. There are a total of 14 lines in this piece of the spectrum without deblending. Panel (c) shows the identified lines and their fits from our reduction method with a deblending algorithm, and panel (d) is the same as (c) except that we use the opacity data instead of the spectral transmission data to fit the saturated lines in order to obtain more accurate values for the equivalent width and the column density. There are a total of 19 lines found with this deblending scheme. We see that without deblending a large percentage (approximately 26%) of lines are missed even for this low spectral cutoff.

In Table 3, we list the properties of several identified lines found in Figure 2 and compare and contrast the methods with and without deblending. Two classes of lines are discussed: single isolated lines, and lines that are blended below a transmission cutoff of  $F_t = 0.7$ . For the unblended lines (#1, 2, and 3), the  $W_0$  and  $N_{\text{HI}}$  differ by about 30–50% between the two methods, and it is evident that equations (8) and (9) give systematically smaller values. The equivalent width computed according to equation (8) is underestimated to a greater degree for lower spectral cutoffs and for weaker lines since the threshold method misses the important contributions to the integral above the cutoff. For the higher spectral cutoffs, this error would get smaller but more lines would be missed since there are many more low column density lines than high column density lines. For the blended lines (#4 and 5), the differences in the two analysis methods are much larger than for the unblended cases. Line #4 is actually a blend of three component lines and line #5 consists of two component lines. The individual components are observed to be a single absorption feature in the threshold method, and the physical parameters of the blended complex of lines are essentially the sum of the deblended component lines.

Figure 3 shows the logarithm of the number of lines (per unit redshift) found in 100 random LOS samples as a function of spectral cutoff for the two methods; with and without deblending. We see that even for low transmission thresholds ( $F_t \leq 0.7$ ), approximately 10 – 30% of lines are missed. For a threshold of 0.95 corresponding to the signal-to-noise ratio of the Keck telescope, the total number of identified lines per unit redshift at  $z = 3$  is 5455 with deblending and 2471 without deblending, which means that roughly 55% of the lines are missed. For higher cutoffs, the situation becomes even worse.

To demonstrate the difference between the deblending and threshold algorithms as well as the effect of different spectral cutoffs, we plot, in Figure 4, the column density distributions for the following four cases:  $F_t = 0.7$  and  $F_t = 0.95$ , each with and without deblending. We see that for  $N_{\text{HI}} \geq 10^{14} \text{ cm}^{-2}$  there are little differences between the different cutoffs and between the different reduction methods. However, at the low column density end, the differences become large (especially considering that Figure 4 is a logarithmic plot). If we take a turn-over in the power-law dependence of the column density distribution as an indication of the completeness limit in the distribution, we find that with deblending and a high cutoff, we are able to achieve completeness down to  $\sim 10^{12} \text{ cm}^{-2}$ . Without deblending, the completeness column density is more than one order of magnitude higher and deviations from the deblending scheme are observed as high as  $3 \times 10^{14} \text{ cm}^{-2}$ . The lack of low column density lines can significantly affect the statistical properties of the Ly $\alpha$  forest. For example, the median Doppler parameter obtained by fitting the Doppler parameters to a Gaussian distribution is  $23.7 \text{ km s}^{-1}$  with deblending and  $21.8 \text{ km s}^{-1}$  without deblending. Also, the slope of the equivalent width distribution  $W^*$ , obtained by fitting to an exponential function, is  $0.11 \text{ \AA}$  with deblending and  $0.25 \text{ \AA}$  without deblending.

Finally, we end this section by noting that observers use several different spectral reduction methods for the QSO absorption lines. Some observers rely on their experience to judge whether or not to deblend a certain line. Others use some automated package such as VPFIT (Carswell 1995) which employs an iterative procedure to minimize the fitting error. For the best comparison to be made between the simulations and the observations, it is imperative that the same procedure be adopted for the analysis of both the simulated and the observed spectra. For now, we have limited ourselves to extracting the actual underlying cloud properties that would be measurable under idealized observational conditions. Certainly the observations are informing us of the true properties of the clouds over some column density range, but at some sufficiently low column density the finite resolution and signal-to-noise of the detectors become limiting factors, as well as the blending of the absorption lines themselves. We have here assumed essentially infinite signal-to-noise and resolution for our spectra, and devised an algorithm for deblending the lines. The deblending is now essential for comparing with the observations of the forest at moderate to high redshifts ( $z > 2$ ) at the high spectral cutoffs ( $F_t > 0.9$ ) that may now be achieved with the high resolution, high signal-to-noise instruments like the Keck HIRES.

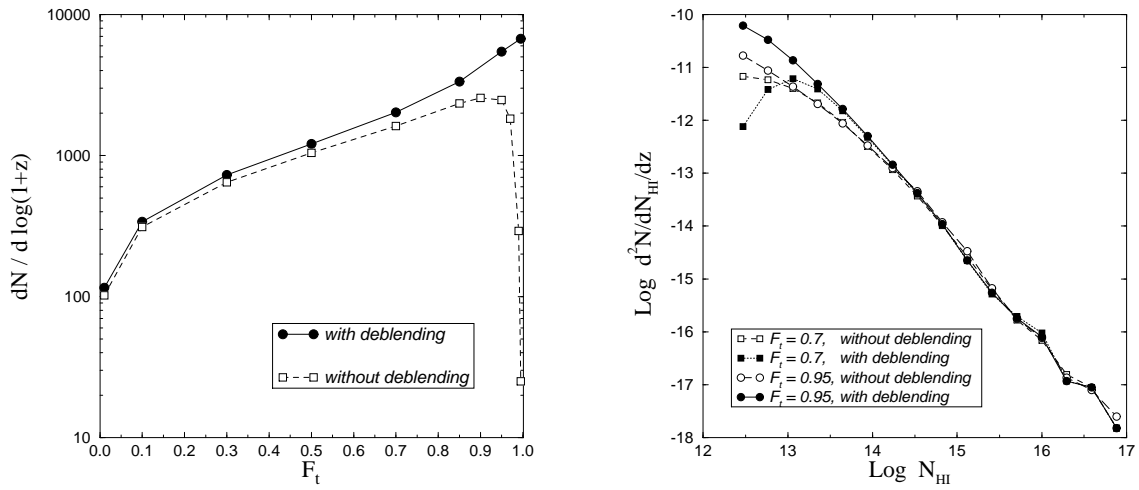


Fig. 3.— The number of identified lines (per unit  $\log(1 + z)$  interval) at  $z = 3$  in 100 random line-of-sight samples is plotted as a function of the spectral cutoff  $F_t$ . The filled circles are results from the deblending spectral analysis method; the open squares represent results from the threshold method. For the typical cutoff  $F_t = 0.95$ , the threshold method misses about 55% of the lines.

Fig. 4.— Column density distributions obtained from the two spectral analysis methods: with (filled symbols) and without (open symbols) deblending. Results from 100 random line-of-sight samples using two different transmission cutoffs,  $F_t = 0.7$  (squares) and  $F_t = 0.95$  (circles), are shown.

#### 4. Spectral Properties at Redshift $z = 3$

In this section, we discuss the statistical properties of the Ly $\alpha$  absorbers at a fixed redshift  $z = 3$ , derived from the spectral analysis method described in §3. As in observations, a particular spectral cutoff is needed to generate a line list from the computed opacity. In order to compare with the highest available resolution data, we employed the same spectral threshold as for the Keck HIRES data,  $F_t = 0.95$ . However, the advantage of numerical simulations is that an arbitrarily high spectral cutoff can be used to make predictions for any improved future observations. It is therefore of interest to use the highest spectral cutoff possible to identify all the lines and derive results from a purely theoretical viewpoint. Hence, in addition to the HIRES cutoff value, we will also present results from the line list obtained by using the low opacity cutoff of  $1 - F_t = 10^{-5}$ , chosen so that it is lower than the minimum opacity at the smallest redshift of our data ( $z = 0.5$ ). The line list with this cutoff thus includes all the generated absorption features.

To create a statistically representative data base, we probe along many randomly directed lines-of-sight (or samples in our case). For each redshift interval,  $\Delta z = 0.1$ , we have generated 913 samples for H I and 500 samples for He II. At  $z = 3$ , for example, the total number of lines in our data set is 73244 for H I and 159630 for He II. The results presented in the following sections are based on the statistics from these large databases.

##### 4.1. Column density distribution

The H I column density distribution is plotted in Figure 5 along with the Petitjean et al. (1993) and Hu et al. (1995) (including their correction for incompleteness) observed data. There is a deficiency of lines between column densities  $10^{15} - 10^{16} \text{ cm}^{-2}$ , compared to the extrapolated power-law fit to lower column density systems, both in the simulation and in the observed distribution (as first noted by Carswell et al. 1987). This deficiency is already apparent in the simulation results using the direct method in ZAN95. The numerical data (filled circles) can be fit to a power law (dotted line) over the entire range of column densities,  $dN/dN_{\text{HI}} \sim N_{\text{HI}}^{-\beta}$  with index  $\beta = 1.70 \pm 0.02$ . It is also of interest to fit the distribution separately at the low and high column density ends. For the Ly $\alpha$  lines with column densities between  $2 \times 10^{12} \text{ cm}^{-2}$  and  $10^{14} \text{ cm}^{-2}$ , the power law index is found to be  $1.39 \pm 0.06$ . For lines with column densities between  $10^{14}$  and  $3 \times 10^{17} \text{ cm}^{-2}$ , the index is  $1.71 \pm 0.03$ . These slopes match the Giallongo et al. (1996) results of 1.4 and 1.8 very well. We are, however, unable to reproduce the observed data at the highest column densities,  $N_{\text{HI}} > \text{few} \times 10^{16} \text{ cm}^{-2}$ . This is likely partly due to the finite computational box size which limits the large scale power, and the finite resolution of the computation, but also because for column densities greater than  $8 \times 10^{16} \text{ cm}^{-2}$ , the opacity at the Lyman edge exceeds 0.5 and self-shielding from the ionizing radiation flux (which we have not included) becomes important. The corrections due to self-shielding can be substantial, without which the neutral hydrogen density can be severely underestimated. Katz et al. (1996) have included a correction for the opacity; nonetheless, even

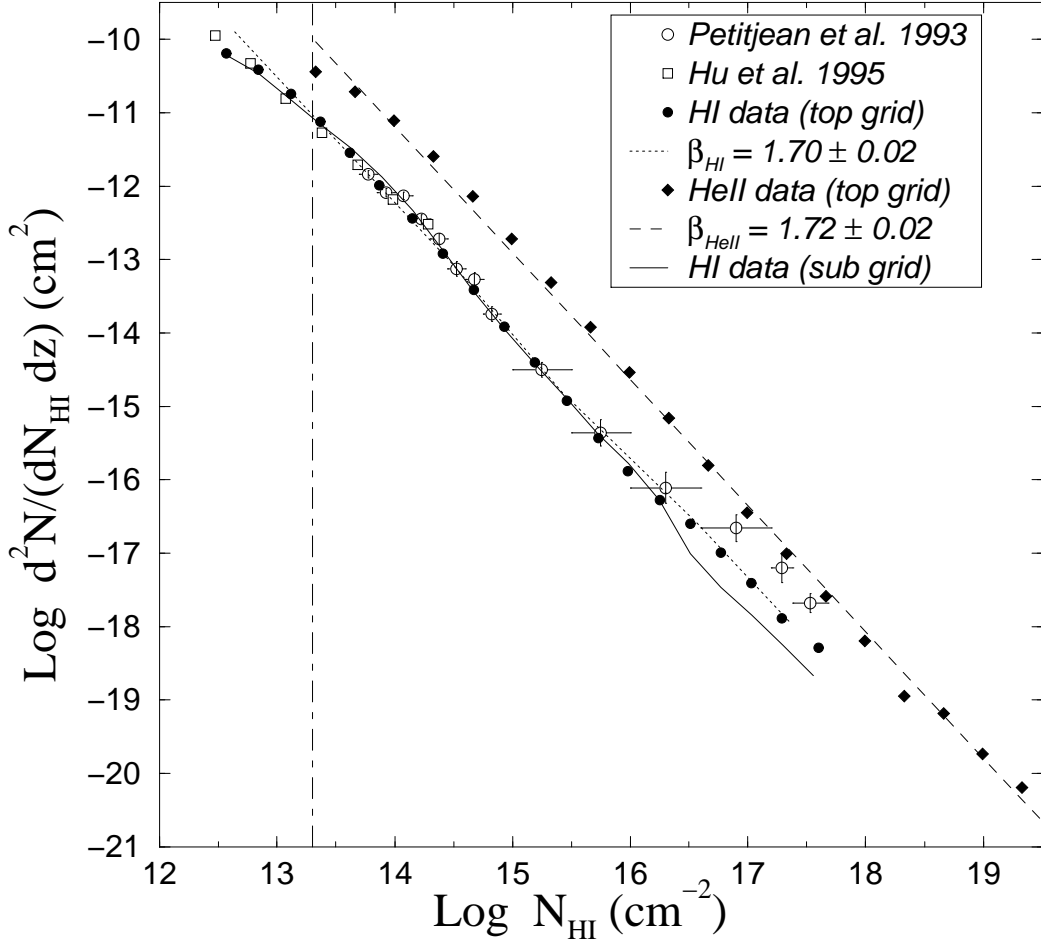


Fig. 5.— H I (filled circles) and He II (filled diamonds) column density distributions at  $z = 3$ . Also shown are the observed data from Petitjean et al. (1993) and Hu et al. (1995). The dotted and dashed lines are the least-squares fits to the entire column density ranges of H I and He II respectively. The H I data can also be fit at the high and low ends with  $\beta = 1.39 \pm 0.06$  for  $2 \times 10^{12} < N_{\text{HI}} < 10^{14} \text{ cm}^{-2}$  and  $\beta = 1.71 \pm 0.03$  for  $10^{14} < N_{\text{HI}} < 3 \times 10^{17} \text{ cm}^{-2}$ . The solid line represents the H I distribution derived from data on the higher resolution sub grid. The vertical dashed line indicates  $N_{\text{HI}} = 2 \times 10^{13} \text{ cm}^{-2}$ , the dividing line between the optically thin and thick components. For the He II distribution, we find  $\beta = 1.72 \pm 0.02$  over the range plotted.

after making the correction, these authors similarly find a significant deficit of high column density systems after matching the normalization to the low column density end. Hence radiative transfer can account for only part of the discrepancy, and it is likely that at least part of the deficit is numerical in origin.

The amplitude of our simulated column density distribution is fixed by our choice of cosmological parameters and the Haardt & Madau (1996) UV radiation field; i.e., no renormalization has been implemented. The overall agreement with observations is excellent, with deviations on the order of 50%. However, the H I column densities (for fixed  $h$ ), scale as the ratio of physical parameters  $b_{\text{ion}}^{\text{HI}} \equiv \Omega_b^2 / \Gamma_{\text{HI},-12}$ , where  $\Gamma_{\text{HI},-12}$  is the photoionization rate at the H I Lyman edge in units of  $10^{-12} \text{ s}^{-1}$ . (The ratio for He II may be similarly defined.) The ratio  $b_{\text{ion}}$  effectively acts as an “ionization bias,” relating the column density of an absorber to its total hydrogen (or helium) column density. This simple scaling arises because neutral hydrogen H I is created by the recombination of protons and electrons, which scales as  $\rho_b^2 \propto \Omega_b^2$ , while also being destroyed by photoionization from the UV radiation, which scales as  $\Gamma_{\text{HI}}$ , over periods of time much shorter than the Hubble time. Note this scaling is valid only to the lowest order when effects such as collisional ionization can be neglected. It also neglects the density dependence of the gas temperature. Provided the cosmological baryon density is not scaled by more than a factor of  $\sim 2$  from the simulation value, the scaling with  $\Omega_b$  is approximately correct. Our choice of model parameters and radiation intensity results in a fortuitous coincidence with the measured number density of systems. We find close agreement with the line density amplitude for  $N_{\text{HI}} > 10^{14} \text{ cm}^{-2}$  found by Davé et al. (1997), after adjusting the two distributions to the same value of  $b_{\text{ion}}$ . We do, however, find significantly more low column density systems. We return to this difference below.

Also shown in Figure 5 is the corresponding He II column density distribution (filled diamonds). This distribution can also be fitted to a power-law, with an index of  $\beta = 1.72 \pm 0.02$  (dashed line). Note again the deficiency of lines in the He II distribution, but in the density range between  $10^{17} - 10^{18} \text{ cm}^{-2}$ .

Finally, we plot the H I column density distribution found on the subgrid of the 9.6 Mpc box (solid line). As mentioned in §2, the more refined subgrid is centered on the most underdense region in the top grid to resolve the lowest column density clouds. For densities below  $10^{16} \text{ cm}^{-2}$ , the top and subgrid results match extremely well, indicating that our results are not sensitive to the spatial grid resolution down to the completeness density of  $\sim 10^{12} \text{ cm}^{-2}$ . The considerably lower amplitude at the very high end ( $> 10^{16} \text{ cm}^{-2}$ ) of the subgrid distribution function is an artifact of centering the subgrid on a void region, and so lacks the highest density fluctuations.

#### 4.2. Doppler parameter distribution

Figure 6 shows the H I and He II Doppler parameter distributions from the simulation. The high resolution Keck HIRES data reveal a lower cutoff to the Doppler parameter with a possible

weak dependence on column density (Hu et al. 1995; Lu et al. 1997). Our data exhibit a similar lower cutoff, with a column density dependence for both the H I and He II data, as shown in Figure 7. The cutoff for the H I case is well fit by  $b_c = 5.5 \log N_{\text{HI}} - 56$  and, expanding for column densities  $N_{\text{HI}} \sim 10^{14} \text{ cm}^{-2}$ , we find  $b_c \approx 15.5 + 5.5 N_{\text{HI}}/10^{14}$ , which compares favorably to the Hu et al. result of  $b_c \approx 16 + 4N_{\text{HI}}/10^{14}$ . The left border is an artifact of setting the threshold for line detection to correspond to  $\tau_0 \approx 0.05$ , which imposes  $b < 1500(N_{\text{HI}}/10^{14}) \text{ km s}^{-1}$  (cf. eq. [12]).

The Doppler parameter obtained from the spectral analysis procedure is significantly smaller than that found using the direct method described in ZAN95. There,  $b$  was computed according to the physical state of the clouds by averaging the temperature and the projected LOS velocity throughout each individual structure. This direct approach is only a crude approximation. Because the H I and He II absorbing regions are generally colder than the entire overdense region selected out through the criteria  $\rho/\bar{\rho} > 1$ , the Doppler parameter can be significantly overestimated, especially for the larger structures. We also note that the Doppler parameter computed from the more sophisticated deblending analysis procedure yields a lower value of  $b$  than the threshold method. The deblending algorithm is able to isolate individual lines within otherwise broader blended features, thereby reducing the line width. A similar difficulty is encountered in the observations, and the trend has been to find a decreasing mean Doppler parameter with increasing spectral resolution and signal-to-noise ratio.

We fit the Doppler parameter distribution to a truncated Gaussian distribution:  $f(b) \propto \exp[-(b - \bar{b})^2/2\sigma^2]$  for  $b > b_{\min}$ , and  $f(b) = 0$  for  $b < b_{\min}$ . We show three fits for H I in Figure 6, with the Gaussian distribution cut off at  $b_{\min} = 0, 15$ , and  $18 \text{ km s}^{-1}$ . We obtain for the respective Gaussian means and widths,  $\bar{b} = 26.1, 25.9$ , and  $25.1 \text{ km s}^{-1}$ , and  $\sigma = 7.0, 7.4$ , and  $8.5 \text{ km s}^{-1}$ . The average Doppler parameter is nearly independent of the assumed cut-off, while the growth in the width reflects the improved fit to the distribution. These values agree well with those of Hu et al. (1995), who, based on Monte Carlo simulations, find that their data at  $z \approx 3$  are adequately described by an underlying truncated Gaussian distribution with  $\bar{b} = 28 \text{ km s}^{-1}$  and  $\sigma = 10 \text{ km s}^{-1}$  for  $b_{\min} = 20 \text{ km s}^{-1}$ . Our results agree somewhat more closely with those of Lu et al. (1997), who find  $\bar{b} = 23 \text{ km s}^{-1}$  and  $\sigma = 8 \text{ km s}^{-1}$  for  $b_{\min} = 15 \text{ km s}^{-1}$ , though these values are for absorbers at  $z \approx 4$ . We find a non-gaussian tail for  $b > 40 \text{ km s}^{-1}$ . A tail is present in the Keck HIRES data as well, but may be due to line-blending, and is reproduced in the Monte Carlo simulations of Hu et al. and Lu et al. We find a log normal distribution,  $f(b) \propto \exp[-\log^2(b/\bar{b})/2\sigma_{ln}^2]$ , with  $\bar{b} = 26.1 \text{ km s}^{-1}$  and  $\sigma_{ln} = 0.27$ , well matches the tail. It also naturally cuts off at low  $b$  without requiring a truncation in the distribution. Our mean Doppler parameter and distribution width for the Gaussian fits are smaller than the values found in the simulations of Hernquist et al. (1996) (but at  $z = 2$ ), for which the threshold method of line-fitting was adopted. Their results agree fairly well with the Gaussian fit Press & Rybicki (1993) inferred from the equivalent width distribution of Murdoch et al. (1986):  $\bar{b} = 32 \text{ km s}^{-1}$  and  $\sigma = 23 \text{ km s}^{-1}$  for  $b_{\min} = 0$ . Even after refitting their lines by Voigt profiles, Davé et al. find a mean  $b$ -value and distribution width at  $z = 3$  that exceed ours. The FWHM of our distribution is  $\sim 20$

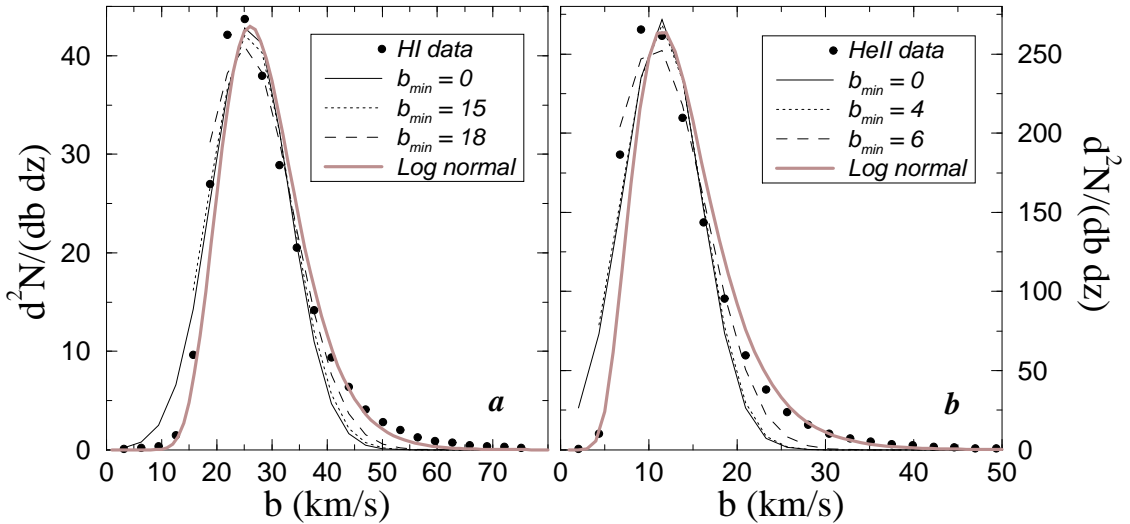


Fig. 6.— Doppler parameter distributions for H I and He II at  $z = 3$ . The filled circles represent numerical data and the different line types are various truncated Gaussian fits with the indicated minimum Doppler parameter. The mean and width for each H I distribution are  $\bar{b} = 26.1, 25.9$ , and  $25.1 \text{ km s}^{-1}$ , and  $\sigma = 7.0, 7.4$ , and  $8.5 \text{ km s}^{-1}$  for  $b_{\min} = 0, 15$ , and  $18 \text{ km s}^{-1}$ , respectively. These agree closely with the Keck HIRES values of  $\bar{b} = 28 \text{ km s}^{-1}$  and  $\sigma = 10 \text{ km s}^{-1}$  for  $b_{\min} = 20 \text{ km s}^{-1}$  at  $z \approx 3$  (Hu et al. 1995), and  $\bar{b} = 23 \text{ km s}^{-1}$  and  $\sigma = 8 \text{ km s}^{-1}$  for  $b_{\min} = 15 \text{ km s}^{-1}$  at  $z \approx 4$  (Lu et al. 1997). The non-gaussian tail for large  $b$  is well captured by a log normal distribution, with  $\bar{b} = 26.1 \text{ km s}^{-1}$ , and dispersion  $\sigma_{ln} = 0.27$ . For He II, we find respectively for  $b_{\min} = 0, 4$ , and  $6 \text{ km s}^{-1}$ ,  $\bar{b} = 11.5, 11.5$ , and  $10.6 \text{ km s}^{-1}$  and  $\sigma = 4.4, 4.5$ , and  $5.8 \text{ km s}^{-1}$ . The log normal parameters are  $\bar{b} = 11.5 \text{ km s}^{-1}$  and  $\sigma_{ln} = 0.38$ .

$\text{km s}^{-1}$ , in close agreement with the Keck data (Hu et al. 1995; Lu et al. 1997). The FWHM of the distribution in Davé et al. is  $\sim 30 \text{ km s}^{-1}$  (their Figure 3). It is unclear at this point whether the disagreement is a consequence of the difference in line analysis software or due to a difference between the simulations.

For the He II Doppler parameter distribution, the values we obtain for the fit parameters with respective cutoffs  $b_{\min} = 0, 4$ , and  $6 \text{ km s}^{-1}$ , are  $\bar{b} = 11.5, 11.5$ , and  $10.6 \text{ km s}^{-1}$ , and  $\sigma = 4.4, 4.5$ , and  $5.8 \text{ km s}^{-1}$ . The mean Doppler parameters are slightly smaller than would be given directly by the scaling of the thermal values,  $(m_{\text{He}}/m_{\text{H}})^{-1/2} = 0.5$ . The reason is that we have used the same threshold cut at  $F_t = 0.95$  for the He II spectra as used for H I. The distribution thus includes, and in fact is dominated by, systems with much lower H I column densities than was used in the H I  $b$ -distribution fit above. These low column density systems appear to be somewhat cooler than their higher column density counterparts. This trend is apparent in Figure 7, which also shows that  $b_c$  for He II is slightly smaller than given by the thermal scaling from the value for  $b_c$  found for the H I at the higher H I column densities. In the region of overlap  $\log N_{\text{HI}} > 12.5$  and  $\log N_{\text{HeII}} > 14.1$  (using  $N_{\text{HeII}}/N_{\text{HI}} \approx 40$  at  $z = 3$  for the Haardt & Madau spectrum), the ratio of  $b_c$ 's is consistent with thermal scaling. The corresponding temperature is  $T \simeq 1.3 \times 10^4 \text{ K}$ . As for the H I, a non-gaussian tail is present. It is well fit by a log normal distribution, with  $\bar{b} = 11.5 \text{ km s}^{-1}$  and  $\sigma_{ln} = 0.38$ .

Pettini (1990) had suggested a possible correlation between the Doppler parameter and column density, but this has not been confirmed by other observers. Figure 7 shows the  $b - N$  scatter plots for H I and He II. Other than for the weak column density dependent lower cutoff in the distribution, there is no apparent correlation in the data. This result is also consistent with the conclusions drawn from the direct method analysis in ZAN95. As shown in ZAN95, the scatter in the data is due, in part, to the broadening of lines from the bulk velocity of the baryonic fluid. This is evident in the low density end, where the gas is at about the same uniform temperature  $\sim 1 \text{ eV}$ . The dispersion of points at low column densities in Figure 7 thus reflects the range of velocities associated with the absorber fluctuations.

#### 4.3. Equivalent width distribution

Observations show that the rest-frame equivalent width distribution can be fit to an exponential relation:  $dN/dW_0 = (N^*/W^*)e^{-W_0/W^*}$ , with  $W^*$  in the range  $0.25 - 0.35 \text{ \AA}$  for the medium resolution observations (Sargent et al. 1980; Murdoch et al. 1986), and in the range  $0.09 - 0.15 \text{ \AA}$  for higher resolution observations (Kulkarni et al. 1996). Overall, our numerical results tend to agree with the higher resolution data, which show a steeper equivalent width distribution.

Figure 8 shows the equivalent width distributions and their exponential fits for both the H I and He II numerical data. We fit an exponential to the data of Hu et al. (1995) for  $W_0 > 0.1 \text{ \AA}$ , and requiring  $N_{\text{HI}} > 10^{13.2} \text{ cm}^{-2}$  (their completeness limit), obtaining  $W^* = 0.17 \pm 0.02 \text{ \AA}$  (95%

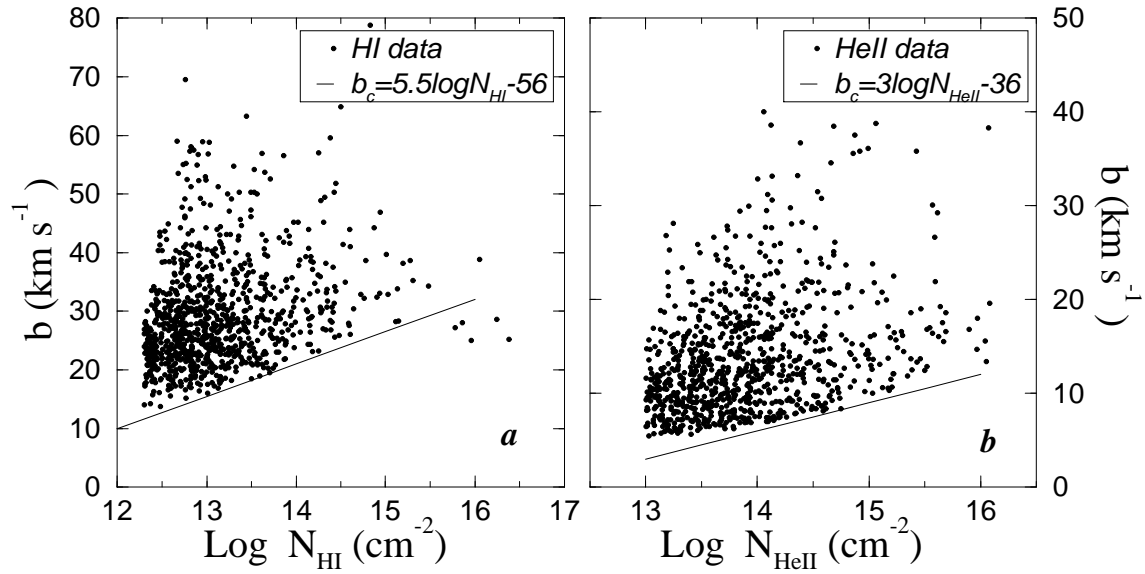


Fig. 7.— Scatter plots of the Doppler parameter versus column density for both H I and He II at  $z = 3$ . We find no apparent correlation between  $b$  and  $N$ . The lower cutoff in the  $b - N_{\text{HI}}$  plot for column densities near  $10^{14} \text{ cm}^{-2}$  is  $b_c = 15.5 + 5.5N_{\text{HI}}/10^{14}$ , derived by expanding the expression in the figure legend around  $N_{\text{HI}} \sim 10^{14} \text{ cm}^{-2}$ . This limit is consistent with the Hu et al. (1995) result  $b_c = 4N_{\text{HI}}/10^{14} + 16$ . The left border is an artifact of setting the threshold for line detection to  $\tau_0 \approx 0.05$ , which imposes  $b < 1500(N_{\text{HI}}/10^{14}) \text{ km s}^{-1}$ .

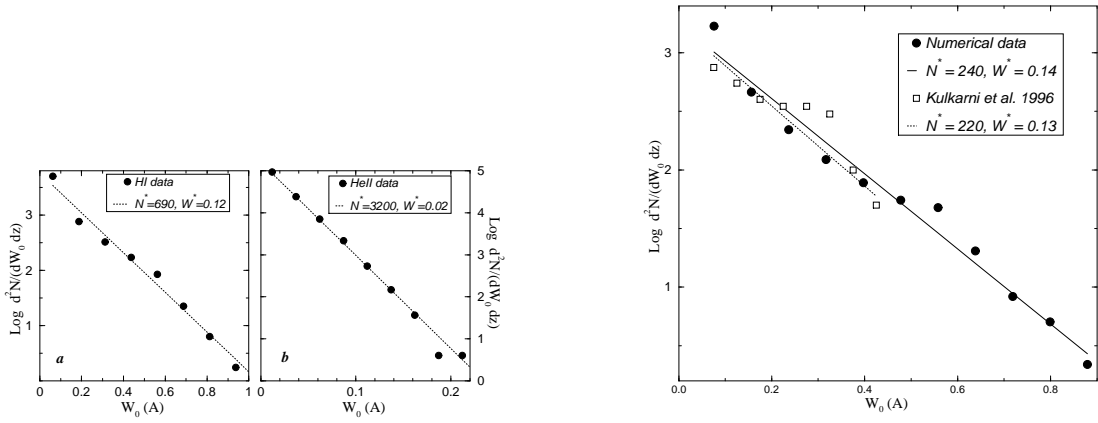


Fig. 8.— Equivalent width distributions for H I and He II at redshift  $z = 3$ . The filled circles represent the numerical data, and the dotted lines are fits to an exponential distribution of the form  $dN/dW_0 = (N^*/W^*)e^{-W_0/W^*}$ . The H I results compare favorably with the Keck HIRES data:  $W^* = 0.17 \pm 0.02 \text{ \AA}$  and  $N^* = 424$ , determined by fitting an exponential to the data of Hu et al. (1995).

Fig. 9.— H I equivalent width distribution at  $z = 2$ . The solid line is the exponential fit to our numerical data, which are represented by filled circles. The dotted line is the exponential fit for the KPNO Q1331+170 data (Kulkarni et al. 1996), indicated by the open squares.

confidence), and  $N^* = 424$  (for an average redshift of  $z = 2.87$ ). The value  $W^* = 0.12 \text{ \AA}$  from the simulation is somewhat smaller, possibly due to missing the higher column density systems as discussed in §4.1 above, but it may be due to incompleteness at low column densities in the HIRES data as well. The line densities of the two distributions agree well. The distribution for He II is much steeper, with an exponent  $W^* = 0.02 \text{ \AA}$  and amplitude  $N^* = 3200$ , which is much higher than the H I case. The He II lines are about 4 times more numerous than the H I lines above their characteristic equivalent widths  $W^*$ .

We also plot the equivalent width distribution at redshift  $z = 2$  along with the KPNO observation of QSO Q1331+170 at  $z \sim 1.9$  (Kulkarni et al. 1996) in Figure 9. The exponential fits to the two data sets, and the corresponding parameters are also displayed. The agreement is excellent in both slope  $W^*$  and amplitude  $N^*$ .

#### 4.4. Line center opacity

We also find the line center opacity can be fit to a power-law distribution of the form  $f(\tau_0) \propto \tau_0^{-\beta}$ , with exponents similar to the column density distribution:  $\beta = 1.64$  and  $1.73$  for H I and He II respectively. Figure 10 shows the H I and He II line center opacity distributions and their respective power-law fits.

Note there is also a slight deficiency of lines with respect to the power-law distribution at  $\log \tau_0 \sim 2$  for H I and  $\log \tau_0 \sim 3$  for He II, which is consistent with the curvature in the column density distribution. The similarity between the column density and line center opacity distributions is understood by noting that  $\tau_0$  is proportional to column density and inversely proportional to the Doppler parameter (cf. eq. [12]). Since the line center opacities and column densities both span about 6 to 8 orders of magnitude, while the Doppler parameter only changes by factors of less than 10, the line center opacity  $\tau_0$  is roughly proportional to  $N_{\text{HI}}$  with the transition from  $\tau_0 < 1$  (optically thin) to  $\tau_0 > 1$  (optically thick) occurring at a column density of  $\log N_{\text{HI}} \approx 13.3$ .

#### 4.5. Metal line systems

An uncertainty that has long-existed in the interpretation of the Ly $\alpha$  forest clouds has been their discreteness. Does a single feature correspond to a single cloud, or are there subcomponents obscured by the finite width of the lines? It has recently become possible to investigate this question observationally by searching for metal absorption in the forest. Since the width of an absorption feature decreases for higher atomic masses when the broadening is predominantly thermal in nature, metal absorption features may act as probes of the internal structure of the forest systems. We explore this possibility using our simulations. Since we do not include any elements other than hydrogen and helium in our simulations, we rescale the hydrogen data by assuming a uniform fractional abundance of the particular element used to generate the spectrum. While the ionization

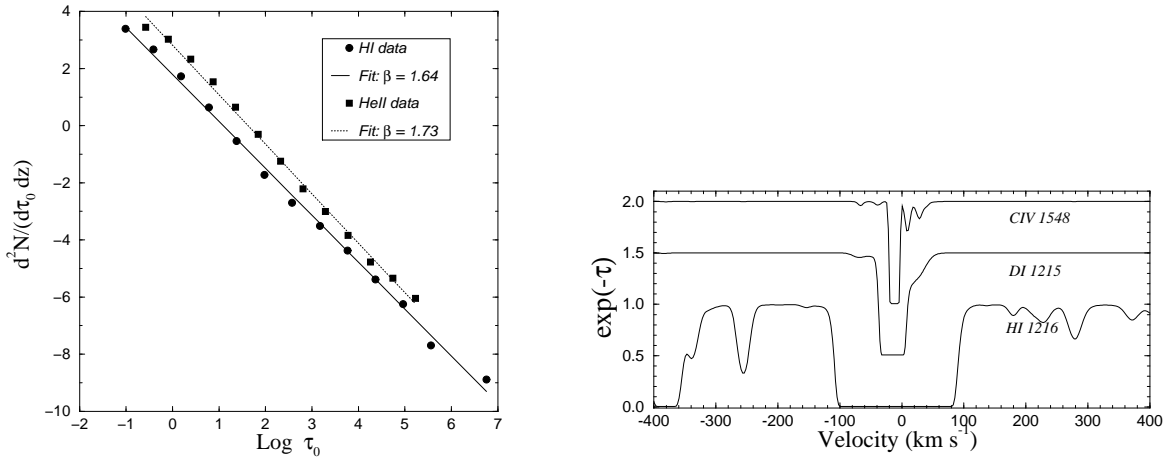


Fig. 10.— Distributions of the line center opacity for H I and He II at  $z = 3$ , and their corresponding power-law fits. The overall shape, deficiency of lines, and fitting exponents are similar to the column density distribution of Figure 5.

Fig. 11.— Characteristic spectra of the D I and C IV absorption line systems. The fractional abundances (relative to neutral hydrogen) are assumed to be  $5 \times 10^{-4}$  (set artificially high for illustration purposes) and  $2 \times 10^{-3}$  for D I and C IV respectively, in accordance with the measurements of Cowie et al. (1995). To prevent the lines from overlapping, the flux transmissions are offset by 0.5 and 1.0 for D I and C IV , respectively.

fractions will generally vary with the internal total gas density of the systems even for a uniform metallicity (e.g., Rauch et al. 1996), here we use the heavier elements simply to indicate substructure within a given hydrogen absorption feature. We consider two heavy elements: deuterium ( $D\,\text{i}\,\lambda 1215$ ) and carbon ( $C\,\text{iv}\,\lambda 1548$ ) with abundances  $n_{D\,\text{i}}/n_{\text{HI}} = 5 \times 10^{-4}$  (set artificially high for illustration purposes), and  $n_{C\,\text{IV}}/n_{\text{HI}} = 2 \times 10^{-3}$ , in accordance with the measurements of Cowie et al. (1995). Figure 11 shows an example of the  $D\,\text{i}$  and  $C\,\text{IV}$  lines located within a saturated  $H\,\text{i}\,\text{Ly}\alpha$  line. The effectiveness of large atomic mass elements to reveal and probe substructure within the broader  $H\,\text{i}$  feature is clear. In particular, we point out that the carbon absorption lines indicate a triplet structure which is a common feature in observed metal line systems (Cowie et al. 1995).

## 5. Evolution Properties

### 5.1. Line Number

Observations have shown that the number of lines larger than a given column density increases with redshift as a power law  $dN/dz \propto (1+z)^\gamma$ . The exact value of  $\gamma$  in numerical simulations will reflect changes in the ionizing radiation, threshold densities or opacities, merging of structures, the expansion rate of the universe, intrinsic line deblending with redshift, and the dependence of the comoving length scale with redshift interval. We may express the evolution in number density of the clouds intercepted along a line-of-sight, above a fixed column density threshold, as

$$\frac{dN}{dz} = \frac{c}{H_0 \lambda_{\text{eff},0}} (1+z)^{1/2} \left( \frac{\Gamma}{\Gamma_0} \right)^{-(\beta-1)} (1+z)^s, \quad (13)$$

where  $\lambda_{\text{eff},0}$  is an effective comoving mean free path between absorbers (scaling like the inverse product of the comoving number density and geometric cross-section of the clouds). The factor  $(1+z)^{1/2}$  includes the  $(1+z)^3$  dilution of the proper number density of the clouds as the universe expands, and the change in the proper length element with redshift (eq. [7] with  $\Omega_0 = 1$  and  $\Omega_\Lambda = 0$ ). The term  $(1+z)^s$  accounts for the evolution in the comoving number density and cross-section of systems corresponding to the column density threshold. For a fixed comoving number density and cross-section,  $s = -2$ . The  $\Gamma$ -dependent factor accounts for the changing column density due to evolution of the radiation field, normalized to the photoionization rate  $\Gamma_0$  at  $z = 0$ . A power-law column density distribution is assumed with exponent  $\beta$ .

Figure 12b shows the evolution of the number of lines (per unit redshift) with different column density cutoffs. Also shown are the total line count for the transmission cutoff  $F_t = 0.95$  (solid line), and the total line count for the minimum opacity cutoff  $1 - F_t = 10^{-5}$  (thick solid line) which represents all the generated lines in the simulation. The thick solid line follows a power-law evolution of the form  $\propto (1+z)^\gamma$  with  $\gamma \approx -1.77 \pm 0.04$ , indicating that the complete absorption line list continues to increase with decreasing redshift. For the complete line list, the  $\Gamma$ -dependence is suppressed (all the lines have been counted), and eq. (13) shows that the clouds evolve with

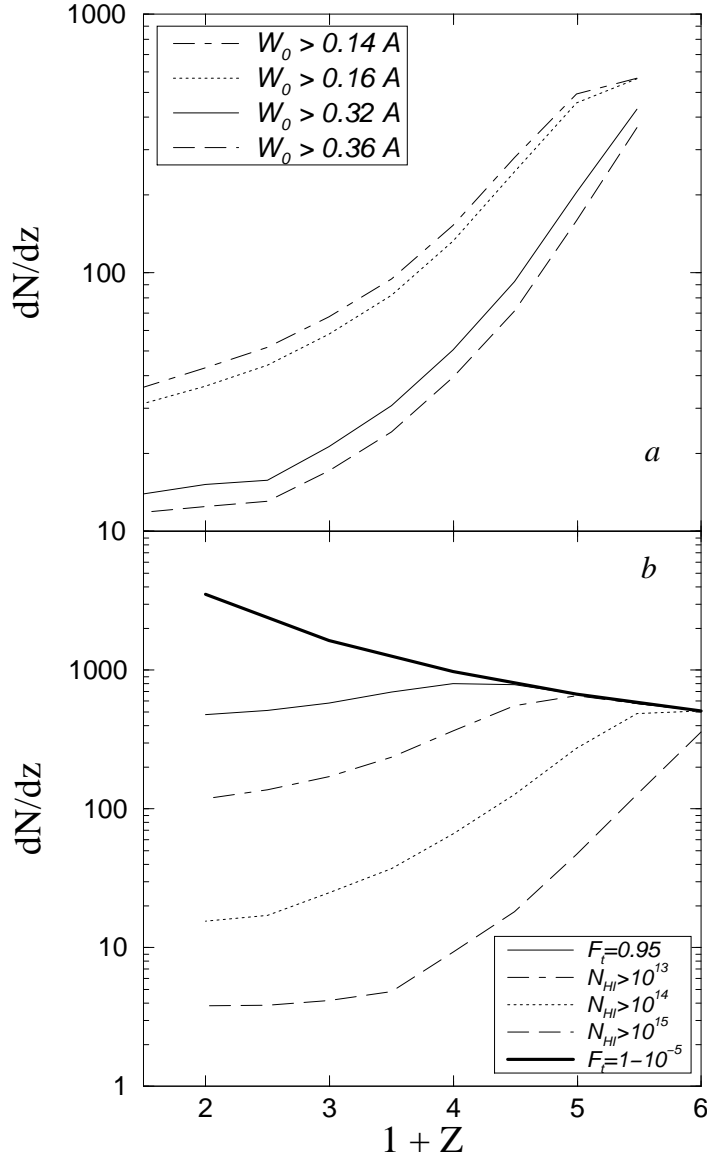


Fig. 12.— Evolution of the number of H I lines with equivalent widths (a) and column densities (b) larger than the displayed values. The lines are identified using a transmission cutoff  $F_t = 0.95$ . In the column density plot, the total line number with this threshold is shown by the solid line, and the thick solid line is the total number of lines obtained with the minimum opacity cutoff  $1 - F_t = 10^{-5}$ , and thus counts all the generated absorption lines, including those that fall above  $F_t = 0.95$ . The thick solid line can be fit to a power-law  $\propto (1 + z)^\gamma$  with  $\gamma \sim -1.77$ .

a nearly constant mean free path in the comoving frame, for which  $\gamma = -1.5$ . The additional factor may be due to the intrinsic blending of spectral features at higher redshifts, which effectively increases the number of lines towards lower redshifts.

There are three notable features in the  $F_t = 0.95$  evolution curves: the duration with which each limiting curve follows the thick solid line increases with smaller density thresholds; the line number count evolves more rapidly at the higher redshifts; and the higher column density clouds exhibit a higher rate of decrease. All three behaviors can be attributed to the evolving radiation field (cf. Figure 1), the fixed transmission cutoff, and the expansion of the universe. For example, at  $z \gtrsim 5$  when the radiation field is low, there is little difference in the number of lines indicated by the different column density thresholds. Thus most of the clouds have column densities above  $10^{15} \text{ cm}^{-2}$ . From  $z \sim 5$  to  $\sim 2$ , the exponential decrease in cloud number reflects the exponential rise in the radiation field. The departure redshift from the thick solid line in Figure 12 is determined by the redshift at which the characteristic line center opacity drops below the threshold opacity associated with the column density cutoffs. Hence, for a fixed transmission cutoff, the exponential cloud number dissipation is triggered at smaller redshifts for the lower density clouds, and since the radiation field evolves less rapidly at the smaller redshifts, the rate of cloud dissipation is less for the lower density thresholds. The expansion of the universe also contributes to the dissipation rate, since the expansion reduces the mean column density and opacity of the IGM. For a fixed transmission cutoff, the number of lines which fall below the threshold increases as the universe expands.

Figure 12a also plots the evolution of the number of lines (per unit redshift) for the different rest frame equivalent width ( $W_0$ ) cutoffs used by observers (cf. Table 4). The characteristic trends found in the column density evolutions are also evident here. Namely, the line number evolves faster in the higher  $W_0$  cutoff cases, and  $dN/dz$  for a fixed  $W_0$  cutoff evolves faster at the higher redshifts. Both effects can be attributed, for the most part, to the changing radiation field.

Table 4 lists the evolution exponents  $\gamma$  calculated for various  $W_0$  limits and redshift ranges, comparing them with the observed values. Note the excellent agreement in each case, except for the high redshift data of Bechtold (1994). To demonstrate the dependence of the evolution exponent on redshift, we compute  $\gamma$  at three separate redshift intervals for clouds with equivalent width cutoff  $W_0 > 0.32 \text{ \AA}$ . We find  $\gamma = 7.70 \pm 0.09$  for  $3.5 < z < 4.5$ ,  $\gamma = 2.95 \pm 0.40$  for  $1.5 < z < 3.5$ , and  $\gamma = 0.24 \pm 0.03$  for  $0.5 < z < 1.5$ . The evolution in our data is much stronger than that indicated by the Bechtold (1994) data, although is only somewhat more rapid than the evolution found using the Keck HIRES data, which we've determined by performing a maximum likelihood fit to the combined line lists of Hu et al. (1995) and Lu et al. (1997). The evolution, however, is sensitive to the evolution of the ionizing UV radiation field, which becomes increasingly uncertain for  $z > 3.5$ . The evolution would be slowed if the UV radiation field declines somewhat less rapidly than given by the Haardt & Madau spectrum, as would be the case if high redshift QSOs were obscured by dust in intervening systems (Fall & Pei 1996). We note that the enhanced rate of evolution we find at higher redshifts agrees with the analysis of Zuo & Lu (1993) for the intrinsic

rate of evolution of the forest, who presume the average Ly $\alpha$  absorption properties arise entirely due to line-blanketing. They suggest a broken power-law for the increase in line density, with a break at  $z = 3.11$ , and  $\gamma_{\text{int}} = 2.82$  below the break and  $\gamma_{\text{int}} = 5.07$  above.

A sequence of column density distributions is shown in Figure 13 at five different redshifts. For this figure, the minimum opacity cutoff of  $10^{-5}$  was used to identify all the absorption features. Because we do not include radiative transfer, the statistics of the distribution for  $N_{\text{HI}} > 10^{17} \text{ cm}^{-2}$  are not directly comparable to observations. We do note, however, that the highest column density systems tend to be associated with the more compact structures. In particular, the damped systems with  $N_{\text{HI}} > 10^{20} \text{ cm}^{-2}$  at  $z = 5$  are associated with dense knots in the gas distribution.

In addition to showing the dissipation and evolution of the clouds, Figure 13 also demonstrates the resolution limitations of our simulations. The turnovers in the distributions indicate the lower density ends at which our numerical absorption line lists become incomplete. This is ultimately tied to the degree of line blending in the spectra (which becomes more severe at higher redshifts) and the cell size of the computational grid. For example, we can estimate the minimum column density resolved in our simulations as the integrated density in a single cell found in the void regions

$$N_{\text{HI},\text{min}} = \Omega_b f_{\text{HI}} \Delta x_c \frac{\rho_b}{\bar{\rho}_b} \frac{\rho_c}{1.4m_p} (1+z)^2, \quad (14)$$

where  $\Omega_b$  is the baryon fraction,  $f_{\text{HI}}$  the neutral hydrogen fraction,  $\Delta x_c$  the comoving cell size,  $\rho_b/\bar{\rho}_b$  the baryonic overdensity in the voids, and  $\rho_c/1.4m_p = (3/8\pi)H_0^2/(1.4Gm_p)$  is the critical comoving number density of hydrogen atoms in a flat expanding universe. For our model parameters, a characteristic underdensity of 0.1 for the voids in which the lowest column density clouds are found (Zhang et al. 1997), and a typical neutral fraction of a few  $\times 10^{-6}$ , we find  $N_{\text{HI},\text{min}} \sim 10^{11} \text{ cm}^{-2}$  at redshift  $z = 3$ , somewhat smaller than the completeness limit of  $\sim 10^{12.5} \text{ cm}^{-2}$ . We also plot in Figure 13 the column density distribution found in the subgrid evolution at the redshift  $z = 3$ , using the same minimum opacity cutoff as the top grid. The distributions match nicely and become incomplete at the same low column densities, suggesting that line blending is the dominant source of incompleteness (for our grid resolutions). A second indication that the turnover is due to incompleteness in the line-identification comes from the He II distribution. The He II distribution turns over only at  $N_{\text{HeII}} < 10^{13.3} \text{ cm}^{-2}$ . For the Haardt & Madau radiation field,  $N_{\text{HeII}}/N_{\text{HI}} \approx 40$  at  $z = 3$ , so that the H I distribution should not turnover until  $N_{\text{HI}} < 10^{11.7} \text{ cm}^{-2}$ , nearly an order of magnitude smaller than the turnover in Figure 13. It is nonetheless possible that the turnovers are partly a reflection of the minimum column density resolvable by the simulation as estimated by equation (14). This may particularly be true for He II, suggesting that the determination of the underlying  $N_{\text{HeII}}$  distribution is at the computational limit.

The distributions in Figure 13 extend somewhat below those of Davé et al. (1997). The difference is particularly noticeable at  $z = 2$ , where we find the column density distribution continues to climb to  $10^{11} \text{ cm}^{-2}$ , more than an order of magnitude smaller than the column density at the peak in their distribution, after accounting for the differences in baryon density and radiation field between the two simulations. We cannot offer a definite explanation for the discrepancy at this

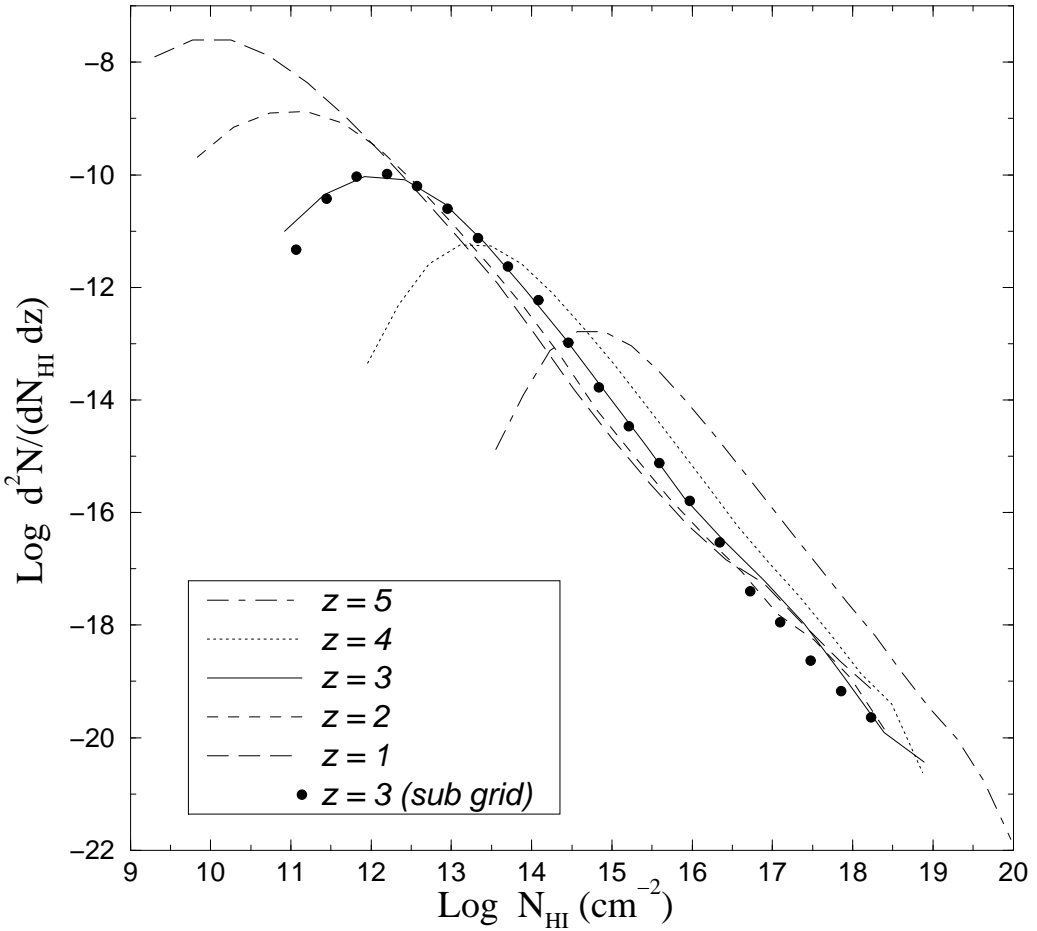


Fig. 13.— Column density distribution at five different redshifts. The minimum opacity cutoff  $1 - F_t = 10^{-5}$  is used to identify all the generated lines in the spectra. The turnover in each curve is an indication of the incompleteness column density. For our grid resolutions, intrinsic line blending is the dominant cause of incompleteness at high redshifts as verified by the sub grid distribution at  $z = 3$ .

point, but it may be due to the differences in the synthesis of the spectra and in the line-finding and fitting algorithms. In particular, since Davé et al. normalize to a higher H I opacity than we do (corresponding to nearly a factor of 2 increase in H I column density for the same physical system compared to our normalization), the difference is likely due in part to blending at low column densities. The analysis approach of Davé et al. is also designed to mimic observational systematics, like noise and the difficulty in estimating a local continuum level, which would lead them to reject the weakest lines. In this sense, the difference may indicate the effect of observational systematics on determining the underlying line distribution. It may, however, also reflect a difference in the effective resolutions of the two codes, particularly in underdense regions where we find most of the low column density systems reside, or of the numerical algorithms themselves. We return to this point in Zhang et al. (1997).

## 5.2. Effective opacity

In spectra of insufficient resolution and signal-to-noise to resolve individual absorption features, the absorption due to the forest will result from the stochastic overlapping of individual lines. If the column density distribution extends down to arbitrarily small values, then the study of absorption by the forest in any spectrum will be resolution-limited at some level. A comparison between the amount of absorption expected from the Ly $\alpha$  forest and the actual amount measured can be used to place a limit on the amount of absorption due to an underlying undetected component, and has been used to set limits on the Gunn-Peterson effect (Steidel & Sargent 1987; Jenkins & Ostriker 1991). It is also an essential quantity for assessing the amount of absorption expected from He II given the observed properties of the H I Ly $\alpha$  forest (Jakobsen et al. 1994; Madau & Meiksin 1994). It is thus of interest to compute the effective opacity in our simulation. The effective opacity due to line blanketing by clouds Poisson distributed in redshift can be calculated from the absorption line distribution  $d^2N/dW_0dz$  as

$$\tau_{\text{eff}} = \frac{1+z}{\lambda_0} \int W_0 \frac{d^2N}{dW_0dz} dW_0 , \quad (15)$$

at redshift  $z$  and Ly $\alpha$  wavelength at rest  $\lambda_0$  (e.g., Press et al. 1993). The flux depression averaged over all lines-of-sight is then  $e^{-\tau_{\text{eff}}}$ .

Figure 14 shows the evolution of the effective opacity contributed by all the H I Ly $\alpha$  absorption lines (for  $F_t = 0.95$ ). The evolution can be fit to an exponential law  $\tau_{\text{eff}} \sim \tau_1 e^{\alpha(1+z)}$ , with  $\tau_1 = 6 \times 10^{-3}$  and  $\alpha = 0.93$ . (The exponential fit is much better than a power-law fit here, as it better approximates the behavior of the radiation field.) We also compute the effective opacity from the published line lists of the four QSOs from Keck HIRES observations at  $z \sim 3$  (Hu et al. 1995), the HIRES observation at  $z \sim 4$  (Lu et al. 1997), and the KPNO observation at  $z \sim 2$  (Kulkarni et al. 1996), using eq. (15), and counting only those lines with line center opacity exceeding 0.05. The results, plotted in Figure 14, agree with our numerical data quite well. To assess the contribution of incompleteness in the line lists, we have recomputed the effective opacities for the

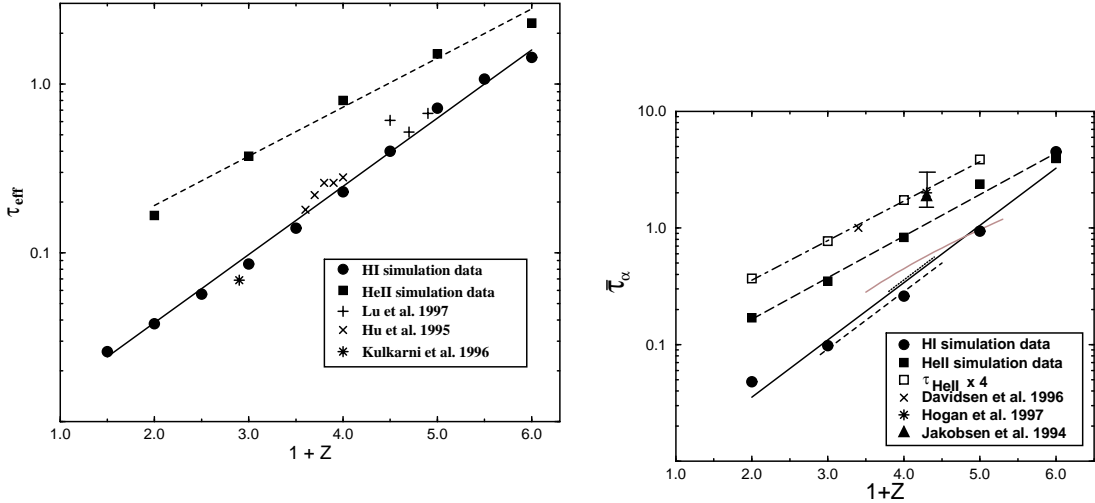


Fig. 14.— Evolution of the effective Ly $\alpha$  opacity from H I and He II line blanketing, using eq. (15) of the text and counting only lines with line center opacity exceeding 0.05. The evolution is well fit by exponentials of the form  $\tau_0 e^{\alpha(1+z)}$  where  $(\tau_0, \alpha)$  are  $(6 \times 10^{-3}, 0.93)$  and  $(5 \times 10^{-2}, 0.67)$  for H I and He II respectively. Also shown are the measured effective opacities using the data taken from the Keck HIRES at  $z \sim 4$  (Lu et al. 1997),  $z \sim 3$  (Hu et al. 1995), and KPNO at  $z \sim 2$  (Kulkarni et al. 1996).

Fig. 15.— Evolution of the average Ly $\alpha$  opacity,  $\bar{\tau}_\alpha \equiv -\log \langle e^{-\tau} \rangle$ . The values for H I are shown by the filled circles. The He II opacities are shown by the filled squares. The open squares show the resulting average opacity after multiplying the He II opacities in the synthetic spectra by a factor of 4. The fit for H I from Press et al. (1993) is shown by the gray solid line. The fit to the absorption measurements of Steidel & Sargent (1987) is shown by the dotted line, and to those of Zuo & Lu (1993) by the short-dashed line (see text). The He II data are taken from Davidsen et al. (1996), Hogan et al. (1997) (95% confidence interval), and the 90% lower limit of Jakobsen et al. (1994). The H I simulation results are fit by  $\bar{\tau}_\alpha^{\text{HI}} = 0.0037e^{1.13(1+z)}$  (solid line). The He II data are fit by  $\bar{\tau}_\alpha^{\text{HeII}} = 0.032e^{0.82(1+z)}$  (dashed line), and  $\bar{\tau}_\alpha^{\text{HeII}} = 0.075e^{0.78(1+z)}$  (dot-dashed line). The average He II opacity at  $z = 5$  for the factor of 4 increase in the spectral opacities coincides nearly with the solid square at  $z = 5$ , and is not included in the fit. The average opacities agree closely with the effective opacities for H I and He II shown in Figure 14, for  $z \leq 3$ , so that almost all the opacity arises from identified absorption lines.

Hu et al. data by weighting each line by the inverse of the incompleteness, as given in their Table 3. The resulting effective opacities increase by at most an additional amount of 0.01–0.02.

Because current measurements of the He II Ly $\alpha$  forest are not able to resolve individual lines, we cannot compare our number counts for the He II Ly $\alpha$  absorbers directly with observations. Higher resolution and more sensitive instrumentation is required. The situation will improve with the installation of the Space Telescope Imaging Spectrograph (STIS) on HST, but at best only the broadest He II absorbers will be resolvable in QSO spectra. We may, however, make an indirect comparison with the data using the effective opacity. The effective opacity for He II from our simulations is shown in Figure 14. The opacity is well fit by an exponential with parameters  $\tau_1 = 5 \times 10^{-2}$  and  $\alpha = 0.67$ .

### 5.3. Average opacity

#### 5.3.1. Simulation Results

In principle, a contribution to the over-all absorption may arise from a component of the IGM that is not readily identified as discrete absorbers. An alternative description of the opacity including all contributions is given by  $\bar{\tau}_\alpha \equiv \log Q_\alpha^{-1}$ , where  $Q_\alpha$  is the observed transmission counting Ly $\alpha$  absorption only (Press, Rybicki, & Schneider 1993). From an analysis of 29 low resolution spectra from the Schneider–Schmidt–Gunn (SSG) QSO survey, Press et al. derive  $\tau_\alpha \approx 0.0037(1+z)^{3.46}$  over the redshift range  $2.5 < z < 4.3$ . In Figure 15, we show the average opacity derived from our spectra, both for H I and He II. The result of Press et al. for H I Ly $\alpha$  is shown as a gray solid line.

A comparison with Figure 14 for the effective opacity due to identified lines alone shows that very little residual opacity is found to arise in the simulation that cannot be fully accounted for by the lines. For  $1 \leq z \leq 3$ , we find  $\bar{\tau}_\alpha - \tau_{\text{eff}} < 0.03$ . The small differences may be due to the difficulty of identifying lines with line center opacity smaller than 0.05. (Only lines with line center opacities exceeding 0.05 were included in our estimate of  $\tau_{\text{eff}}$ .) At higher redshifts the difference increases. It is difficult to assess at this point, however, whether the additional absorption is due to gas that has not condensed into absorbing clouds or to incompleteness in the line finding as a result of line-blending at these high redshifts. By comparison, the Press et al. estimate for  $\bar{\tau}_\alpha$  at  $z = 3$  is 0.45, exceeding the simulation results by 70%. The direct line count of the Hu et al. (1995) data (shown in Figure 14), gives  $\tau_{\text{eff}} = 0.28$ . This resurrects an old problem identified by Jenkins & Ostriker (1991): the opacities from the SSG QSO spectra greatly exceed those due to line blanketing based on direct line counting from higher resolution spectra. Here we point out that the discrepancy persists for line lists based on the much higher resolution, higher signal-to-noise spectra from the Keck HIRES. Recomputing  $\bar{\tau}_\alpha$  for the Keck data would substantially help to clarify the origin, or reality, of this discrepancy. One possibility is that the difference is an artifact of the low resolution (25Å) of the SSG spectra, which could result in an overestimate of the continuum level

by failing to resolve emission features longward of the QSO Ly $\alpha$  emission line (Steidel & Sargent 1987). The higher resolution data (6Å) of Steidel & Sargent (1987) result in systematically lower opacities than derived from the SSG data. We return to this point in the following section.

There are two QSO lines-of-sight for which measurements of intergalactic He II absorption have been published. At  $z \approx 3.3$ , Jakobsen et al. (1994) obtain  $\tau > 1.7$  (90% confidence), while, for the same QSO sightline, Hogan et al. (1997) find  $1.5 < \tau < 3$  (95% confidence). For a second line-of-sight, Davidsen et al. (1996) obtain  $\tau = 1.0 \pm 0.07$  ( $1\sigma$ ), at  $\langle z \rangle \approx 2.4$ . We show these limits in Figure 15, along with  $\bar{\tau}_\alpha$  for He II computed from the simulation. The measured values substantially exceed those of the simulation. The difference may be accounted for by increasing the size of the break at the He II Lyman edge, but would require a decrease by a factor of  $\sim 4$  of the estimate for the He II ionization rate from Haardt & Madau (1996) (shown by the open boxes). While this would be consistent with the break that would result from a soft QSO spectrum (Madau & Meiksin 1994), it is fairly large, and would require a steep intrinsic QSO spectrum, with  $\alpha_Q \approx 1.8 - 2$ . Alternatively,  $\Omega_b$  may be increased, and additional sources of H I ionizing photons postulated to prevent too large a value for  $\tau_{\text{eff}}$  due to line-blanketing from the neutral hydrogen. This would require a doubling of  $\Omega_b$  to 0.12, a high value but still in keeping with the Big Bang nucleosynthesis constraints imposed by measurements of deuterium in high redshift absorption systems (Tytler et al. 1996). The agreement of the H I simulation results with the observed redshift trend of  $\tau_{\text{eff}}$  in Figure 14, however, would then in part be fortuitous.

### 5.3.2. Comparison with TreeSPH

We compare our opacity results with those of Croft et al. (1997), based on a similar SCDM simulation, but using TreeSPH. We summarize the comparison in Table 5. For  $\Omega_b = 0.06$  and the Haardt & Madau spectrum, the ionization bias for H I in our simulation is  $b_{\text{ion}}^{\text{HI}} = 0.0035$  at  $z = 2$  and  $b_{\text{ion}}^{\text{HI}} = 0.0038$  at  $z = 3$ . For the parameters chosen by Croft et al. for their dynamical run ( $\Omega_b = 0.05$ , half the Haardt & Madau rates),  $b_{\text{ion}}^{\text{HI}} = 0.0052$  at  $z = 2$  and 3. They find for their run  $\bar{\tau}_\alpha^{\text{HI}} = 0.16$  at  $z = 2$ , and 0.41 at  $z = 3$  (from their Figure 3b). Scaling the opacities in our spectra to  $b_{\text{ion}}^{\text{HI}} = 0.0052$  (and assuming no temperature correction), we find  $\bar{\tau}_\alpha^{\text{HI}} = 0.13$  at  $z = 2$  and 0.32 at  $z = 3$ . We thus find only fair agreement with Croft et al. : their values exceed ours by 25–30%. For He II, our simulation ran with  $b_{\text{ion}}^{\text{HeII}} = 0.31$  at  $z = 2.4$  and 0.42 at  $z = 3.3$ . The simulation of Croft et al. ran with  $b_{\text{ion}}^{\text{HeII}} = 0.47$  at  $z = 2.4$  and  $b_{\text{ion}}^{\text{HeII}} = 0.59$  at  $z = 3.3$ . They find  $\bar{\tau}_\alpha^{\text{HeII}} = 0.73$  at  $z = 2.4$  and  $\bar{\tau}_\alpha^{\text{HeII}} = 2.0$  at  $z = 3.3$ . For the same values of the ionization bias (and no temperature correction), we obtain  $\bar{\tau}_\alpha^{\text{HeII}} = 0.63$  at  $z = 2.4$  and 1.3 at  $z = 3.3$ . We thus find a discrepancy in the He II opacities as well: the values in Croft et al. exceed ours by 15–50%.

It is possible that much of the discrepancy is due to differences in the gas temperatures. Such a difference may arise as a consequence of the different ionization histories adopted by the two simulations, particularly in the underdense regions, where most of the He II opacity is generated. An increase in temperature lowers the radiative recombination rates to H I and He II, and so reduces

their respective column densities for the same total gas density. Both simulations, however, produce comparable temperatures, 7000–15000 K, over the range of densities dominating the H I opacity (overdensities of a few). Still, a 50% change in temperature will alter the column densities by 30%, so temperature differences may play some role in accounting for the different opacities. A second possibility is that the higher Doppler parameters found in the TreeSPH simulation compared to ours (§4.2), reflects a true underlying difference between the simulations. The larger  $b$ –values would broaden the saturated lines, increasing their contribution to the average opacity in direct proportion to the ratio of Doppler parameters. The mean SPH  $b$ –value is  $\sim 30\%$  larger than ours, so that the difference in the Doppler parameter distributions may account for a large part of the discrepancy in the opacities.

There is a significant difference in temperatures in the underdense regions. The TreeSPH simulation finds  $T \lesssim 6000$  K (Katz et al. 1996). Our simulation shows a spread in temperatures over approximately 6000 – 8000 K for the underdense gas at  $z = 3$  (Zhang et al. 1997). The temperature in the underdense regions is particularly susceptible to details of the ionization history because the density is too low for the gas to maintain the temperature at the photoionization thermal equilibrium value. Allowing for the increase in the radiative recombination rate on changing the temperature from 8000 K to 6000 K, the “temperature corrected” average opacity values from our simulation are  $\bar{\tau}_\alpha^{\text{HeII}} = 0.71$  at  $z = 2.4$  and 1.5 at  $z = 3.3$ . The value at  $z = 2.4$  now compares very favorably with the SPH calculation, although a 30% discrepancy still remains at  $z = 3.3$ .

The temperature dependence of the average opacity actually does not scale quite so simply, since the absorption profile of the distribution of the absorbing atoms is sensitive to the temperature as well. We may assess the effect of a change in temperature quantitatively when the average opacity is dominated by line–blanketing, as we in fact find is the case. The opacity is then given by the average equivalent width of the lines (cf., eq. [15]). For optically thin clouds, the equivalent width scales linearly with the column density, hence with the radiative recombination rate (the linear part of the curve–of–growth). For saturated absorption, however, the equivalent width scales in direct proportion to the Doppler parameter, and becomes nearly insensitive to the column density and recombination rate (Spitzer 1978). Since the line–blanketing opacity is dominated by saturated lines, the temperature sensitivity will be suppressed. Indeed, depending on the distribution of line center opacities in the forest, an increase in gas temperature could even result in an *increase* in the average opacity. We may derive the temperature dependence from eq. (15), where we substitute a distribution over line center opacity  $\tau_0$  for the distribution over rest equivalent width  $W_0$ . Assuming a power law opacity distribution with slope  $\beta$ , and using eqs. (10) – (12), we obtain (assuming the integration range may be extended from 0 to  $\infty$ ),

$$\tau_{\text{eff}} \propto \alpha_R^{\beta-1} b^{2-\beta}, \quad (16)$$

where  $\alpha_R$  is the radiative recombination coefficient to either H I or He II. Over the temperature range of interest,  $\alpha_R \propto T^{-0.7}$ . For thermally broadened lines,  $b \propto T^{1/2}$ . We then find for H I, with  $\beta = 1.64$ ,  $\tau_{\text{eff}} \propto T^{-0.27}$ . For He II, with  $\beta = 1.73$ , we obtain  $\tau_{\text{eff}} \propto T^{-0.38}$ . We find that this relation results nearly exactly in the temperature scaling for the He II average opacity found above.

Although an opacity difference of 30% may not seem large, because of the weak dependence of opacity on  $b_{\text{ion}}$  it translates into a substantial difference in the requirements for the background ionization field. Normalized to the same value of  $\Omega_b$ , we find we need to reduce the Haardt & Madau estimate of the He II ionizing background by an additional factor of 1.5–2 above the requirements of Croft et al. in order to match to the He II observations. It is critical to resolve the formation of structures on small scales to ensure convergence to the correct opacity. The clumping of gas into clouds that produce saturated or nearly saturated absorption features opens up regions in the spectrum of low optical depth, and so increases the average transparency. Since most of the He II absorption arises in structures that are underdense, we believe it likely that the difference in resolution between the two simulations is in part responsible for the discrepancy in opacities. While our resolution at  $z = 3$  is 18.75 kpc on the top grid, the resolution in the lowest density regions is  $\sim 200$  kpc in the SPH simulation (Hernquist et al. 1996). We provide a more extensive discussion of the distribution of opacity in Zhang et al. (1997).

#### 5.4. Flux decrement

A particularly useful wavelength range to measure the flux decrement due to the forest is between Ly $\alpha$  and Ly $\beta$  in the restframe of the QSO. This region avoids Ly $\beta$  absorption by the forest, enabling an estimate for the decrement based solely on Ly $\alpha$  absorption. Oke & Korycansky (1982) define the flux decrement  $D_A$  as

$$D_A = \frac{32}{5} \frac{1}{1 + z_Q} \int_{(27/32)(1+z_Q)-1}^{z_Q} [1 - \exp(-\tau_\nu)] dz, \quad (17)$$

where  $z_Q$  is the redshift of the QSO. (In practice, an upper wavelength somewhat short of Ly $\alpha$  is chosen to avoid the broad wing of the QSO Ly $\alpha$  emission line. Here, we retain the full wavelength range. The difference should be small.) Figure 16 plots the evolution of the H I  $D_A$  from  $z = 5$  to  $z = 1$  along with an exponential fit to the data of the form  $D_A = D_A^0 e^{\alpha(1+z)}$ , with  $D_A^0 = 0.01$  and  $\alpha = 0.75$ . Also shown are four different measurements of the  $D_A$  decrement from Steidel et al. (1987), Schneider et al. (1991), Zuo & Lu (1993), and Kennefick et al. (1995). Despite the rather large scatter in the observational data, the agreement with the simulation results is fairly good, although the measured values of Schneider et al. are systematically higher than the numerical data. However, these data are predominantly derived from low resolution spectra (25Å), and the improved continuum accuracy permitted by higher resolution observations can lower their values, as discussed by Steidel & Sargent (1987), who obtained 6Å resolution data. The values reported by Zuo & Lu were estimated by performing new continuum fits to the  $\sim 1$ Å resolution data of Sargent et al. (1988). (We use only the estimates from their Table 1, based on a direct integration of the digital spectra.) In any event, the numerical results (for both the column density distribution and  $D_A$  evolution), may be made to match the observations more precisely by adjusting the physical parameters of our simulations, either by changing the radiation intensity or the baryon density. In particular, the more rapid fall off in the values measured by Zuo & Lu toward lower redshifts than

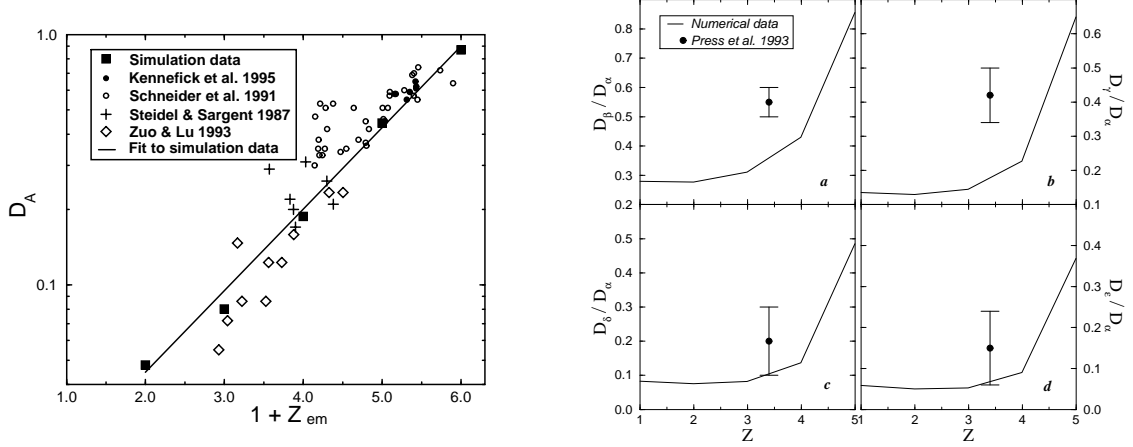


Fig. 16.— Evolution of the H I flux depression  $D_A$  between Ly $\alpha$  and Ly $\beta$ , as a function of the emission redshift of the QSO. Also shown are four separate observations and an exponential fit to the numerical data,  $D_A = 0.01e^{0.75(1+z)}$ .

Fig. 17.— Evolution of the average H I flux depression ratios for the first several Lyman series transitions: a)  $D_\beta/D_\alpha$ , b)  $D_\gamma/D_\alpha$ , c)  $D_\delta/D_\alpha$  and d)  $D_\epsilon/D_\alpha$ . Also shown with filled circles and error bars are the values determined from the Press, Rybicki, & Schneider (1993) analysis of the Schneider, Schmidt, & Gunn (1991) data at  $z \sim 3.4$ . Their derived ratios of effective opacities translate to  $D_\beta/D_\alpha = 0.55 \pm 0.05$ ,  $D_\gamma/D_\alpha = 0.42 \pm 0.08$ ,  $D_\delta/D_\alpha = 0.20 \pm 0.10$ , and  $D_\epsilon/D_\alpha = 0.15 \pm 0.09$ .

given by the simulation would be consistent with the onset of additional sources of H I ionizing radiation at  $z < 3$ , such as young massive stars in forming galaxies.

We may use the  $D_A$  estimates of Steidel & Sargent (1987) and Zuo & Lu (1993) to estimate the mean intergalactic opacity  $\tau_\alpha$  as a function of redshift. We do so by setting  $\tau_\nu = \tau_\alpha(z)$ , where  $\nu = \nu_\alpha/(1+z)$ , in eq.(17). For the Steidel & Sargent data, we attempted to fit their 7 measurements (we exclude the measurement of the BAL QSO), by the relations  $\tau_\alpha = A(1+z)^{3.46}$  and  $\tau_\alpha = Ae^{\beta(1+z)}$ , and minimizing  $\chi^2$  using their estimate of 0.05 for the error in  $D_A$ . We found neither form was able to give an acceptable fit. The reason was due to an anomalously large  $D_A$  value at  $z = 2.57$ . Removing this point, we obtain  $\tau_\alpha = 0.0028(1+z)^{3.46}$  and, fixing  $\beta = 1.13$  to match the simulation fit,  $\tau_\alpha = 0.0039e^{1.13(1+z)}$ , both with acceptable values for  $\chi^2$ . (Varying the redshift evolution rates did not much improve  $\chi^2$ .) For the 10  $D_A$  measurements in Table 1 of Zuo & Lu, we obtain  $\tau_\alpha = 0.0022(1+z)^{3.46}$  and  $\tau_\alpha = 0.0031e^{1.13(1+z)}$ , both with acceptable  $\chi^2$  values. We show the fits in Figure 15.

Press, Rybicki, & Schneider (1993) compute the average flux decrements of the first several Lyman series transitions (Ly $\beta$ , Ly $\gamma$ , Ly $\delta$  and Ly $\epsilon$ ) relative to the Ly $\alpha$  average flux decrement. They express their results in terms of ratios of the mean equivalent widths (normalized by the rest wavelength of the respective transition), or equivalently, in terms of the ratios of the mean opacities  $\bar{\tau}_\alpha$ ,  $\bar{\tau}_\beta$ , etc. These ratios are computed from our simulation by scaling the line center opacities by the appropriate oscillator strengths and wavelengths. Each average opacity is meant to include the absorption contribution due to a single component of the Lyman series. In analogy to  $D_A$ , we may define  $D_i = 1 - e^{-\bar{\tau}_i}$  for the  $i^{th}$  term of the Lyman series. Hence,  $D_\alpha = D_A$ . The results are plotted as a function of redshift in Figure 17. Also shown are the corresponding calculations by Press, Rybicki, & Schneider (1993) for the observed data of Schneider, Schmidt, & Gunn (1991) at  $z \sim 3.4$ , reexpressed in terms of the flux decrements  $D_i$ . The observed values are higher than our predicted numbers, especially for the Ly $\beta$  and Ly $\gamma$  transitions. For a pure power-law column density distribution for the Ly $\alpha$  forest, it is straightforward to show that the ratios of  $\bar{\tau}$ 's (when convergent), are given by  $\bar{\tau}_i/\bar{\tau}_\alpha = (\lambda_i f_i / \lambda_\alpha f_\alpha)^{\beta-1}$ . Thus, the difference is likely a reflection of the steeper column density distribution found in the simulations compared to the rather flat distribution inferred from the Schneider et al. data: Press & Rybicki (1993) obtain  $\beta = 1.43 \pm 0.04$ . It is noteworthy that our results for these ratios agree well with those of Miralda-Escudé et al. (1996), especially considering that the cosmological models and adopted radiation fields are different in the two simulations.

## 6. Summary

We have developed a spectral synthesis and analysis procedure, based on fitting the absorption features to Voigt profiles. The procedure is capable of resolving the lowest (as well as the higher) column density absorption features in numerical simulations. We have applied our procedures to several numerical simulations of the Ly $\alpha$  forest in a standard CDM model with a self-consistent

treatment of the dark matter, the baryonic matter, a chemical reaction network of hydrogen and helium components, radiative cooling, and the Haardt & Madau (1996) ionizing radiation field based on QSOs as the dominant sources of the radiation. With the adequate modeling of microphysical and radiation processes, we are able to reproduce the essential observational data down to the completeness H I column densities of our simulations, approximately  $10^{12} \text{ cm}^{-2}$  at redshift  $z = 3$ . The advances in our line analysis methods are essential in resolving the low density, optically thin H I Ly $\alpha$  features, especially for comparing results to recent high resolution observed data such as taken by the Keck HIRES. We find excellent agreement with the observed data for our adopted simulation parameters, including the slopes and shapes of the column density and equivalent width distributions, the value and distribution of Doppler parameters, and the evolutionary histories of the line number, flux decrement, and opacities. We comment that we cannot reproduce both the high H I mean opacity estimate of Press et al. (1993) and the H I effective opacity due to line-blanketing. The Press et al. opacity substantially exceeds the opacity due to line-blanketing as determined directly from the line lists obtained using the Keck HIRES. We find instead that the average opacity in the simulation agrees very closely to the line-blanketing opacity for  $1 \leq z \leq 3$ , with  $\bar{\tau}_\alpha - \tau_{\text{eff}} < 0.03$  over this redshift range. It is possible that the low resolution of the spectra analyzed by Press et al. resulted in an overestimate of the average intergalactic H I opacity. We find good agreement with the values of the average flux decrement  $D_A$  measured by Steidel & Sargent (1987), Zuo & Lu (1993), and Kennefick et al. (1995), over the redshift range  $2 \lesssim z \lesssim 5$ , as well as with the mean intergalactic Ly $\alpha$  opacity we infer from these values. Since the opacity is sensitive to the intensity of the UV photoionizing background, the agreement over the wide redshift range is noteworthy, and supports QSOs as the dominant sources of the ionizing radiation field.

The evolution in the H I line number density we obtain is somewhat too rapid compared to observations at the highest redshifts ( $z > 3.5$ ). The rate of evolution, however, is sensitive to the assumed evolution of the radiation field, which becomes increasingly uncertain at these redshifts. We are able to match the normalization in the number counts of the Ly $\alpha$  forest systems at the low column density end ( $N_{\text{HI}} \lesssim 14 \text{ cm}^{-2}$ ) assuming the Haardt & Madau QSO-dominated UV radiation background and a baryon density consistent with standard nucleosynthesis limits, but curvature in the distribution results in a significant deficit of lines at the high end ( $N_{\text{HI}} > \text{few} \times 10^{16} \text{ cm}^{-2}$ ). It is possible, however, that the discrepancy is due to the finite box size and resolution of the simulation (and the neglect of self-shielding effects for the very high column densities), rather than an intrinsic consequence of SCDM.

We have explored the effects of grid resolution by performing analogous statistical calculations of the Ly $\alpha$  absorbers on higher resolution grids and found that our results are not sensitive to cell size at the low column density end, down to the completeness column density limit. We find that (for our spatial grid resolutions) intrinsic line blending is the dominant cause of incompleteness in the generated line lists at high redshifts. The grid resolution (or, in the case of SPH calculations, the effective resolution defined by particle counts in the void regions) can be important in setting the completeness density at smaller redshifts.

We compare our results with those of a similar simulation with nearly identical cosmological parameters and power-spectrum performed by Hernquist et al. (1996) using TreeSPH, as re-analyzed by Davé et al. (1997) using Voigt profiles and by Croft et al. (1997) for the opacity distributions. While there is generally good agreement between the two simulation results, we find that a power-law H I column density distribution extends to substantially lower column densities than they find. We also find somewhat lower Doppler parameters and a narrower Doppler parameter distribution, in agreement with Keck HIRES measurements. Because Davé et al. introduce observational systematics into their spectra in order to mimic the measured spectra, while we work directly with the opacity assuming no observational systematics, much of the discrepancy is likely due to the differences in the analysis procedures. We nonetheless do find some differences in the analysis-independent average opacities, as given by Croft et al. The TreeSPH average H I opacities exceed our values by 25–30%, and the He II opacities by up to 50%. The discrepancies can be accounted for in part by the different ionization histories adopted for the two simulations, and the resulting differences in gas temperatures and ionization fractions. The differences, however, may also be due in part to the lower resolution of the TreeSPH calculation.

The He II opacities we obtain are substantially smaller than those measured. We are able to reach agreement with the observations by reducing the He II ionizing background by a factor of 4 relative to the estimate of Haardt & Madau (1996). The smaller intensity requires a soft intrinsic QSO spectrum, with  $\alpha_Q \approx 1.8 - 2$ .

Although we have not pursued a detailed analysis of cloud morphologies in this paper, we do note that the geometrical shapes of the clouds are found to be linked to the local thermal and gravitational environments (see also Miralda-Escudé et al. 1996). Spheroidal clouds are concentrated at the intersections of the filaments which commonly form in CDM-like models, and are typically more massive (and gravity confined) than the elongated clouds which tend to lie along the filament strands. Our simulations also indicate that a significant percentage of low column density absorption lines come from local density enhancements in the underdense void regions. Further investigations of cloud morphologies and “minivoid” absorption features are presented in a companion paper (Zhang et al. 1997).

We are pleased to thank Ed Bertschinger, Renyue Cen, Lars Hernquist, Jorje Miralda-Escudé, Jerry Ostriker, and David Weinberg for useful conversations, and Martin White for helpful comments. This work is supported in part by the NSF under the auspices of the Grand Challenge Cosmology Consortium (GC<sup>3</sup>). The computations were performed on the Convex C3880 and the SGI Power Challenge at the National Center for Supercomputing Applications, and the Cray C90 at the Pittsburgh Supercomputing Center under grant AST950004P. A.M. thanks the William Gaertner Fund at the University of Chicago for support.

## REFERENCES

- Abel, T., Anninos, P., Zhang, Y., & Norman, M. L. 1996, New Astronomy, submitted
- Anninos, P., Norman, M. L., & Clarke, D. A. 1994, ApJ, 436, 11
- Anninos, P., Zhang, Y., Abel, T., & Norman, M. L. 1996, New Astronomy, submitted
- Arons, J. 1972, ApJ, 172, 553
- Bahcall, J. N., & Salpeter, E. E. 1965, ApJ, 142, 1677
- Bahcall, J. N. et al. 1993, ApJS, 87, 1
- Bahcall, J. N. et al. 1996, ApJ, 457, 19
- Bajtlik, S., Duncan, R. C., & Ostriker, J. P. 1988, ApJ, 327, 570
- Bardeen, J. M., Bond, J. R., Kaiser, N., & Szalay, A. S. 1986, ApJ, 304, 15
- Bechtold, J. 1994, ApJS, 91, 1
- Bertschinger, E. 1995, astro-ph/9506070
- Bi, H., Ge, J., & Fang, L. Z. 1995, ApJ, 452, 90
- Black, J. H. 1981, MNRAS, 197, 553
- Bond, J R., & Myers, S. T. 1996, ApJS, 103, 63
- Bond, J. R., Szalay, A.S. & Silk, J. 1988, ApJ, 324, 627
- Carswell, R. F. 1995, private communication
- Carswell, R. F., Webb, J. K., Baldwin, J. A., & Atwood, B. 1987, ApJ, 319, 709
- Cen, R., Miralda-Escudé,J., Ostriker, J. P., & Rauch, M. 1994, ApJ, 437, L9
- Charlton, J., Anninos, P., Zhang, Y., & Norman, M. L. 1996, ApJ, submitted (astro-ph/9601152)
- Copi, C. J., Schramm, D. N., & Turner, M. S. 1995, Science, 267, 192
- Cowie, L. L., Songaila, A., Kim, T. S., & Hu, E. M. 1995, AJ, 109, 1522
- Cristiani, S., D’Odorico, S., Fontana, A., Giallongo, E., & Savaglio, S. 1995, MNRAS, 273, 1016
- Croft, R. A. C., Weinberg, D. H., Katz, N., & Hernquist, L. 1997, ApJ, submitted (astro-ph/9611053)
- Davé, R., Hernquist, L., Weinberg, D. H., & Katz, N. 1997, ApJ, in press (astro-ph/9609115)

- Davidsen, A., Kriss, G. A., & Zheng, W. 1996, *Nature*, 380, 47
- Dinshaw, N., Foltz, C. B., Impey, C. D., Weymann, R. J., & Morris, S. L. 1995, *Nature*, 373, 223
- Fall, S. M., & Pei, Y. C. 1993, *ApJ*, 402, 479
- Fang, Y., Duncan, R. C., Croots, A. P. S., & Bechtold, J. 1996, *ApJ*, 462, 77
- Giallongo, E. 1991, *MNRAS*, 251, 541
- Giallongo, E., Cristiani, S., D'Odorico, S., Fontana, A., & Savaglio, S. 1996, *ApJ*, 466, 46
- Haardt, F. & Madau, P. 1996, *ApJ*, 461, 20
- Hernquist, L., Katz, N., Weinberg, D., & Miralda-Escudé, J. 1996, *ApJ*, 457, L51
- Hogan, C. J., Anderson, S. F., & Rugers, M. H. 1997, submitted (astro-ph/9609136)
- Hu, E. M., Kim, T. S., Cowie, L. L., Songaila, A., & Rauch, M. 1995, *AJ*, 110, 1526
- Ikeuchi, S. 1986, *Ap&SS*, 118, 509
- Ikeuchi, S. & Ostriker, J.P. 1986, *ApJ*, 301, 522
- Jakobsen, P., Boksenberg, A., Deharveng, J. M., Greenfield, P., Jedrzejewski, R., & Paresce, F. 1994, *Nature*, 370, 35
- Jenkins, E. B., & Ostriker, J. P. 1991, *ApJ*, 376, 33
- Katz, N., Weinberg, D., & Hernquist, L. 1996, *ApJS*, 105, 19
- Katz, N., Weinberg, D., Hernquist, L., & Miralda-Escudé, J. 1996, *ApJ*, 457, L57
- Kennefick, J.D. et al. 1995, *AJ*, 110, 78
- Kulkarni, V. P., Huang, K., Green, R. F., Bechtold, J., Welty, D. E., & York, D. G. 1996, *MNRAS*, 279, 197
- Lu, L., Sargent, W. L. W., Womble, D. S., & Takada-Hidai, M. 1997, *ApJ*, in press (astro-ph/9606033)
- Lu, L., Wolfe, A. M., & Turnshek, D. A. 1991, *ApJ*, 367, 19
- Lynds, C. R. 1971, *ApJ*, 164, L73
- Madau, P., & Meiksin, A. 1994, *ApJ*, 433, L53
- Meiksin, A. 1994, *ApJ*, 431, 109
- Miralda-Escudé, J., Cen, R., Ostriker, J. P., & Rauch, M. 1996, *ApJ*, in press (astro-ph/9511013)

- Murdoch, H. S., Hunstead, R. W., Pettini, M., & Blades, J. C. 1986, ApJ, 309, 19
- Oke, J.B., & Korycansky, D.G. 1982, ApJ, 255, 11
- Ostriker, J.P., & Ikeuchi, S. 1983, ApJ, 268, L63
- Petitjean, P., Webb, J. K., Rauch, M., Carswell, R. F., & Lanzetta, K. 1993, MNRAS, 262, 499
- Pettini, M., Hunstead, R. W., Smith, L., & Mar, D. P. 1990, MNRAS, 246, 545
- Press, W. H., Rybicki, G. B., & Schneider, D. P. 1993, ApJ, 414, 64
- Press, W. H., & Rybicki, G. B. 1993, ApJ, 418, 585
- Rauch, M., Haehnelt, M. G., & Steinmetz, M. 1997, ApJ, in press (astro-ph/9609083)
- Rees, M.J. 1986, MNRAS, 218, 25
- Rees, M.J. 1988, in *QSO Absorption Lines*, eds. J.C. Blades, D.A. Turnshek & C.A. Norman (Cambridge University Press)
- Sargent, W. L. W., Boksenberg, A., & Steidel, C. C. 1988, ApJS, 68, 539
- Sargent, W. L. W., Young, P. J., Boksenberg, A., & Tytler, D. 1980, ApJS, 42, 41
- Schneider, D.P., Schmidt, M., & Gunn, J.E. 1991, AJ, 101, 2004
- Smette, A., Robertson, J. G., Shaver, P. A., Reimers, D., Wisotski, L., & Koehler, T. 1995, A&AS, 113, 199
- Spitzer, L. 1978, *Physical Processes in the Interstellar Medium* (New York: John Wiley & Sons)
- Steidel, C.C., & Sargent, W.L.W. 1987, ApJ, 313, 171
- Tytler, D., Fan, X-M, & Burles, S. 1996, Nature, 381, 207
- White, S. D. M., Efstathiou, G., & Frenk, C. S. 1993, MNRAS, 262, 1023
- Zhang, Y., Anninos, P., & Norman, M. L. 1995, ApJ, 453, L57
- Zhang, Y., Meiksin, A., Anninos, P., & Norman, M. L. 1997, ApJ, in preparation
- Zuo, L., & Lu, L. 1993, ApJ, 418, 601

Run	$\Omega_0$	$\Omega_b$	$h$	$\sigma_{8h^{-1}}$	$L$ (Mpc)	$\Delta x$ (kpc)	$M_b(M_\odot)$	$\Delta M_b(M_\odot)$	$\Delta M_d(M_\odot)$
9.6–Top	1	0.06	0.5	0.7	9.6	75	$3.7 \times 10^{12}$	$1.8 \times 10^6$	$2.9 \times 10^7$
9.6–Sub	1	0.06	0.5	0.7	9.6	18.75	$5.8 \times 10^{10}$	$2.7 \times 10^4$	$4.6 \times 10^5$
3.2–Top	1	0.04	0.7	1.0	3.2	25	$1.8 \times 10^{11}$	$8.5 \times 10^4$	$1.7 \times 10^7$
3.2–Sub	1	0.04	0.7	1.0	3.2	6.25	$2.8 \times 10^9$	$1.3 \times 10^3$	$2.7 \times 10^5$

Table 1: The physical and computational parameters of the different Ly $\alpha$  forest simulations.  $\Omega_0$  is the cosmological density parameter,  $\Omega_b$  the baryonic mass fraction,  $h$  the Hubble parameter,  $\sigma_{8h^{-1}}$  the fluctuation normalization in a sphere of radius  $8h^{-1}$  Mpc,  $L$  the comoving box size,  $\Delta x$  the comoving cell size,  $M_b$  the total baryonic mass in the simulation,  $\Delta M_b$  the initial mass of baryons in a single cell and  $\Delta M_d$  the dark matter particle mass. The “Top” and “Sub” in the run labels refer to the top or sub grid calculations. We use  $128^3$  cells for both the top and sub grids, and a refinement factor of 4, hence the effective grid resolution of the sub grids is  $512^3$ . Results for the small box, high amplitude model were reported in ZAN95.

Instrument	$\Delta z$	$\Delta v$ (km s $^{-1}$ )	$\Delta\lambda_{\text{HI}}$ (Å)	$\Delta\lambda_{\text{HeII}}$ (Å)
numerical spectrum	$2 \times 10^{-6}$	0.6	$\sim 0.01$	$\sim 0.002$
KECK/HIRES	$(1.8 \sim 2.8) \times 10^{-5}$	$5.3 \sim 8.4$	$0.09 \sim 0.14$	N/A
KPNO/KPE	$6 \times 10^{-5}$	18	$\sim 0.3$	N/A
ASTRO-2/HUT	$2.5 \times 10^{-3}$	750	N/A	3
HST/FOC	$1.6 \times 10^{-2}$	5000	N/A	20

Table 2: The spectral resolution in our numerical data is shown along with some relevant observational instruments. The wavelength resolutions are calculated in the observer’s frame for a typical redshift  $z = 3$ . N/A is entered in the table when the relevant wavelength range is not covered by the instrument. Our spectral resolution is more than adequate to cover the grid cell intervals, which, at  $z = 3$ , are  $\Delta z = 1 \times 10^{-4}$  and  $2.5 \times 10^{-5}$  for the top and sub grids respectively.

Line #	Threshold method				Deblending method			
	$v$ (km s $^{-1}$ )	$N$ (cm $^{-2}$ )	$W_0$ (Å)	$b$ (km s $^{-1}$ )	$v$ (km s $^{-1}$ )	$N$ (cm $^{-2}$ )	$W_0$ (Å)	$b$ (km s $^{-1}$ )
1	3328.2	2.2e14	0.09	33.8	3328.2	3.1e14	0.14	33.7
2	3519.6	7.9e12	0.04	24.2	3519.6	1.5e13	0.07	24.2
3	4106.4	1.3e13	0.06	30.3	4106.4	2.1e13	0.10	30.3
4	4392.2	1.2e15	1.15	168.5	4301.6	4.2e14	0.36	25.2
					4449.7	7.2e14	0.64	45.6
					4608.8	2.0e13	0.09	23.5
5	5146.4	9.9e13	0.32	66.4	5112.6	6.8e13	0.21	24.6
					5185.7	4.0e13	0.17	40.3

Table 3: The spectral properties of a few typical lines (extracted from Figure 2) as derived from the threshold and deblending methods. Lines #1–3 are single isolated features; lines #4 and #5 are blended below the transmission cutoff  $F_t = 0.7$ .  $v$  is the line center position in velocity space,  $N$  is the extracted column density,  $W_0$  the equivalent width, and  $b$  the Doppler parameter.

$\gamma$	$W_0$ limit (Å)	Redshift interval	Observations
$2.83 \pm 0.40$	0.36	1.5 – 3.5	$2.75 \pm 0.29$ (Lu et al. 1991)
$5.28 \pm 0.60$	0.32	2.5 – 4.0	$1.89 \pm 0.28$ (Bechtold 1994)
$5.28 \pm 0.60$	0.32	2.5 – 4.0	$3.19 \pm 0.76$ (Hu et al. 1995; Lu et al. 1997)
$2.95 \pm 0.40$	0.32	1.5 – 3.5	$2.31 \pm 0.40$ (Murdoch et al. 1986)
$0.24 \pm 0.03$	0.32	0.5 – 1.5	$0.60 \pm 0.62$ (Bahcall et al. 1993)
$0.45 \pm 0.01$	0.24	0.5 – 1.5	$0.42 \pm 0.42$ (Bahcall et al. 1996)
$4.84 \pm 0.36$	0.16	2.5 – 4.0	$1.32 \pm 0.24$ (Bechtold 1994)
$4.84 \pm 0.36$	0.16	2.5 – 4.0	$3.28 \pm 0.49$ (Hu et al. 1995; Lu et al. 1997)
$2.81 \pm 0.41$	0.14	1.5 – 3.5	$2.15 \pm 0.51$ (Giallongo 1991)

Table 4: A comparison between the exponent  $\gamma$  for the line number evolution in our numerical simulations, and in several different observations. The exponent is tabulated as a function of the minimum equivalent width ( $W_0$ ) cutoff, and the redshift interval is chosen to match the different observations.

H I Opacity				He II Opacity			
$z$	$b_{\text{ion}}$	$\bar{\tau}_{\alpha}^{\text{sim}}$	$\bar{\tau}_{\alpha}^{\text{SPH}}$	$z$	$b_{\text{ion}}$	$\bar{\tau}_{\alpha}^{\text{sim}}$	$\bar{\tau}_{\alpha}^{\text{SPH}}$
2	0.0035	0.10	...	2.4	0.31	0.49	...
	0.0052	0.13	0.16	2.4	0.47	0.63	0.73
				2.4	0.47	0.71*	0.73
				2.4	1.2	1.1	...
3	0.0038	0.26	...	3.3	0.42	1.1	...
	0.0052	0.32	0.41	3.3	0.59	1.3	2.0
				3.3	0.59	1.5*	2.0
				3.3	1.7	2.2	...

Table 5: A comparison between the average opacity found in our simulations,  $\bar{\tau}_{\alpha}^{\text{sim}}$ , and that found by Croft et al. (1997),  $\bar{\tau}_{\alpha}^{\text{SPH}}$ , based on a similar SCDM simulation but using TreeSPH. The values marked by an asterisk for HeII take into account the possible effect of the difference in gas temperatures between the two simulations (see text).